Published in "Journal of Comparative Neurology 525(15): 3266–3285, 2017"
which should be cited to refer to this work.

Parvalbumin-expressing ependymal cells in rostral lateral ventricle wall adhesions contribute to aging-related ventricle stenosis in mice

Federica Filice[1] | **Marco R. Celio**[1] | **Alexandre Babalian**[1] | **Walter Blum**[1,2] | **Viktoria Szabolcsi**[1]

[1]Anatomy and Program in Neuroscience, Department of Medicine, University of Fribourg, Fribourg, Switzerland

[2]INSERM UMR-1162, Génomique Fonctionelle des Tumeurs Solides, Paris, France

Correspondence
Viktoria Szabolcsi, Anatomy and Program in Neuroscience, Department of Medicine, University of Fribourg, Rte. A. Gockel 1, Fribourg CH-1700, Switzerland.
Email: viktoria.szabolcsi@unifr.ch

Funding information
Swiss Multiple Sclerosis Society, Grant/Award Number: 2016-28; Forschungsfonds of the University of Fribourg, Grant/Award Number: 582

Abstract

Aging-associated ependymal-cell pathologies can manifest as ventricular gliosis, ventricle enlargement, or ventricle stenosis. Ventricle stenosis and fusion of the lateral ventricle (LV) walls is associated with a massive decline of the proliferative capacities of the stem cell niche in the affected subventricular zone (SVZ) in aging mice. We examined the brains of adult C57BL/6 mice and found that ependymal cells located in the adhesions of the medial and lateral walls of the rostral LVs upregulated parvalbumin (PV) and displayed reactive phenotype, similarly to injury-reactive ependymal cells. However, PV+ ependymal cells in the LV-wall adhesions, unlike injury-reactive ones, did not express glial fibrillary acidic protein. S100B+/PV+ ependymal cells found in younger mice diminished in the LV-wall adhesions throughout aging. We found that periventricular PV-immunofluorescence showed positive correlation to the grade of LV stenosis in nonaged mice (<10-month-old), and that the extent of LV-wall adhesions and LV stenosis was significantly lower in mid-aged (>10-month-old) PV-knock out (PV-KO) mice. This suggests an involvement of PV+ ependymal cells in aging-associated ventricle stenosis. Additionally, we observed a time-shift in microglial activation in the LV-wall adhesions between age-grouped PV-KO and wild-type mice, suggesting a delay in microglial activation when PV is absent from ependymal cells. Our findings implicate that compromised ependymal cells of the adhering ependymal layers upregulate PV and display phenotype shift to "reactive" ependymal cells in aging-related ventricle stenosis; moreover, they also contribute to the progression of LV-wall fusion associated with a decline of the affected SVZ-stem cell niche in aged mice.

KEYWORDS
aging, ependymal cell, lateral ventricle, parvalbumin, ventricle stenosis, RRID:AB_10000344, RRID:AB_2665495, RRID:AB_2315304, RRID:AB_2620025, RRID:AB_1555288, RRID:AB_221569, RRID:AB_221568, RRID:AB_839504, RRID:SCR_002526, RRID:SCR_002285, RRID:SCR_002798

1 | INTRODUCTION

In a previous article, we described the injury-triggered upregulation of the EF-hand calcium-binding protein parvalbumin (PV) in ependymal cells of the lateral ventricle (LV) (Szabolcsi & Celio, 2015). This study investigates the effects of aging on ependymal cells and the ependymal-cell responses in aging-associated ventricle stenosis known for its deleterious effects on adult neurogenesis in old mice.

Adult neurogenesis takes place in two regions of the mammalian brain: in the subgranular zone of the dentate gyrus (Kaplan & Hinds, 1977) and in the subventricular zone (SVZ) along the lateral wall of the rostral LV (Lois & Alvarez-Buylla, 1994). The SVZ supports neurogenesis by continuously generating new neurons that migrate to the olfactory bulb via the rostral migratory stream (Doetsch & Alvarez-Buylla, 1996). The SVZ is a neurogenic stem cell niche with a unique microenvironment consisting not only of neural stem cells (NSCs) but support

cells and blood vessels. The ventricle surface in the adult neurogenic niche is organized in pinwheels with centrally located NSCs that contact the ventricle via apical processes, surrounded by ependymal cells (Mirzadeh, Merkle, Soriano-Navarro, Garcia-Verdugo, & Alvarez-Buylla, 2008). SVZ-supported neurogenesis has been shown to considerably decrease with aging (Tropepe, Craig, Morshead, & van der Kooy, 1997), and this decline is in part due to a reduction in epidermal growth factor receptor signaling (Enwere et al., 2004), but other factors are likely involved, too. The morphological changes in the aging SVZ involve a reduction in the number of pinwheels, of NSCs per pinwheel, and of ventricle-containing apical processes of the NSCs (Shook, Manz, Peters, Kang, & Conover, 2012). One unique characteristic of aging is ventral stenosis of the LV walls, which is formed by adhesion and later on fusion of the medial and lateral LV walls, causing the deterioration of the affected SVZ, therefore most of the ventral neurogenic SVZ (Luo, Daniels, Lennington, Notti, & Conover, 2006; Shook et al., 2012). As a result of this, and/or additional age-associated alterations, the rest of the ventricular cavity expands; causing a thinning of the remaining ependymal cell layer (Conover & Shook, 2011).

The ventricular system is lined with ependymal cells that form a cell monolayer, facilitate the circulation of cerebrospinal fluid (CSF) and participate in the metabolic exchange between CSF and brain parenchyma (Del Bigio, 2010). Ependymal cells in the brain, unlike other epithelial linings, display inadequate regeneration following lesion since they are unable to generate progeny required for the replacement of cell loss (Spassky et al., 2005). A form of SVZ-mediated ependyma repair throughout aging is retained by astrocytes that integrate in the ependymal layer and take on morphological features of ependymal cells (Luo, Shook, Daniels, & Conover, 2008). Other studies revealed that in the neurogenic SVZ stem cell niche, the two main niche cell types, ependymal cells, and astrocytes retained a high level of plasticity: in response to lesion, astrocytes gave rise to ependymal cells and ependymal cells gave rise to niche astrocytes (Nomura, Goritz, Catchpole, Henkemeyer, & Frisen, 2010). Recently, we have found an alternative mechanism of ependymal-cell response to injury: ependymocytes following mechanical lesion acquired reactive phenotype, enhanced cell motility and wound-closure capacity upon injury-induced PV-upregulation (Szabolcsi & Celio, 2015).

Ependymal-cell pathologies involve a wide variety of diseases and conditions ranging from genetic disorders resulting in hydrocephalus (Del Bigio, 2010), declined adult neurogenesis via loss of planar cell polarity (Sawamoto et al., 2006) or ankyrin 3 (*Ank3*) (Paez-Gonzalez et al., 2011), and impaired barrier function leading to leukocyte infiltration into the ventricles in infectious and inflammatory conditions (Alvarez & Teale, 2007). Because of the restricted regenerative capacity of ependymal cells, deleterious impulses that compromise the ependymal layer often result in irreversible loss of ependymal integrity, a phenomenon that occurs throughout aging both in human and mice (Shook et al., 2013). Aging-related ependymal cell loss implies ventricular surface gliosis and consequent ventricle enlargement—a condition often observed in elderly humans (Shook et al., 2013), revealing the importance of maintaining an intact ependymal cell lining throughout aging.

During the course of ventricle stenosis, the ependymal layer is essentially intact in the adhered LV walls in 3-month-old mice, but deteriorates throughout aging as fusion progresses, leaving 1-year-old mice without ependymal cells in the fused regions (Shook et al., 2012). Most importantly, SVZ-supported neurogenesis is also absent in fused LV walls lacking ependymal cells, thereby extensive LV-wall fusions contribute fundamentally to the aging-related decline of SVZ-supported neurogenesis (Shook et al., 2012). Despite its impact, the molecular and cellular players underlying the progression of LV-wall fusion are so far unknown.

This study was undertaken to learn more about the role ependymal cells play in the progression of aging-related LV-wall fusion and ventricle stenosis and to determine what role ependymal PV-expression might play in this process.

2 | MATERIALS AND METHODS

2.1 | Mice

C57BL/6 (Janvier, Lyon, France), Parvalbumin-Cre::loxP-DsRed-loxP-enhanced green fluorescent protein (eGFP) (hereafter: PV-Cre/eGFP), PV-KO, PV-KO-eGFP, and Foxj1-eGFP mice (Jackson Laboratory, Bar Harbor, ME) were used in this study. Mice that express *Cre* under the *Pvalb* promoter were crossed with a double-fluorescent, Cre-reporter strain [B6;C3-Tg(CAG-DsRed,-EGFP)5Gae/J; Jackson Laboratory, Sacramento, CA], which has a general expression of a loxP-flanked red fluorescent protein variant (DsRed-Express) prior to Cre recombinase exposure, and eGFP following Cre-mediated recombination. In the offspring, the DsRed-Express cassette is deleted in the PV-expressing cells, allowing expression of the eGFP cassette located downstream. PV-KO-eGFP mice were generated by crossing a PV-eGFP mouse strain (B6.Tg(Pvalb-EGFP)1Hmon) to a PV-KO one (B6.Pvalbtm1SwalXB6Tg(Pvalb-EGFP)1Hmon) (Schwaller et al., 1999). Foxj1-eGFP mice [(B6;C3-Tg(FOXJ1-EGFP)85Leo/J, Jackson Laboratory, Sacramento, CA] express eGFP under the control of the human forkhead box J1 (*Foxj1*) gene promoter, a transcription factor known as the master regulator of motile ciliogenesis (Ostrowski, Hutchins, Zakel, & O'Neal, 2003). In the murine brain, Foxj1-expression is restricted to ependymal cells and a subset of astrocytes in the adult stem cell niche in the SVZ (Jacquet et al., 2009). All animal experiments were performed according to institutional guidelines and with the permission of the cantonal committee on animal experimentation (Permission No: 2016_03_FR).

2.2 | Immunofluorescence

Adult C57BL/6 ($n = 15$), PV-Cre/eGFP ($n = 6$), Foxj1-eGFP ($n = 8$), PV-KO ($n = 18$), and PV-KO-eGFP ($n = 5$) mice (4- to 15-month-old, of both sexes) were transcardially perfused with a solution of 4% paraformaldehyde (PFA) in 0.1M phosphate-based saline (PBS, pH 7.4). The brains were removed and post-fixed in 4% PFA in PBS overnight at 4°C, followed by incubation overnight in a cryoprotectant solution (18% saccharose in Tris-based saline [TBS]), and processed for cutting

TABLE 1 List of the antibodies and antisera used in this study

Name	Immunogen	Manufacturer, Cat. no., RRID	Species	Clonality	Dilution for IF	Dilution for WB
anti-PV	Recombinant mouse parvalbumin	Swant, GP72, RRID:AB_2665495	Guinea-pig	Polyclonal	1:1,000	1:5,000
anti-PV	Recombinant rat parvalbumin	Swant, PV 25, RRID:AB_10000344	Rabbit	Polyclonal	1:1,000	1:5,000
anti-GFAP (5C10)	Purified pig spinal cord GFAP	Novus Biologicals, NBP1–05197, RRID:AB_1555288	Mouse	Monoclonal	1:1,000	1:1,000
anti-S100B	Purified bovine brain S100B	Swant, 37, RRID:AB_2315304	Rabbit	Polyclonal	1:1,000	1:1,000
anti-S100B	Recombinant full length rat S100B	Synaptic Systems, 287 004, RRID:AB_2620025	Guinea-pig	Polyclonal	1:500	1:1,000
anti-Iba1	Synthetic peptide corresponding to C-terminus of Iba1	WAKO, 019–19741, RRID:AB_839504	Rabbit	Polyclonal	1:1,000	1:1,000
anti-GFP	Jellyfish *A. victoria* GFP	Thermo Fisher Scientific, A-11122, RRID:AB_221569	Rabbit	Polyclonal	1:2,000	1:5,000
anti-GFP	Jellyfish *A. victoria* GFP	Thermo Fisher Scientific, A-11120, RRID:AB_221568	Mouse	Monoclonal	1:2,000	1:2,000

IF = immunofluorescence; WB = Western blot

40-μm-thick coronal sections with a freezing microtome (Frigomobil, Reichert-Jung, Vienna, Austria). Immunofluorescence was performed on free-floating sections with the following antibodies and antisera (Table 1): rabbit anti-PV (diluted 1:1,000, Swant, Marly, Switzerland, Cat. #PV 25, RRID:AB_10000344), guinea pig anti-PV (diluted 1:1,000, Swant, Marly, Switzerland, Cat. #GP72, RRID:AB_2665495), rabbit anti-S100B (diluted 1:1,000, Swant, Marly, Switzerland, Cat. #37, RRID:AB_2315304), guinea pig anti-S100B (diluted 1:500, Synaptic Systems, Göttingen, Germany, Cat. #287 004, RRID:AB_2620025), mouse anti-glial fibrillary acidic protein (GFAP) (diluted 1 μg/ml, Novus Biologicals, Cambridge, UK, Cat. #NBP1–05197, RRID:AB_1555288), rabbit anti-GFP (diluted 1 μg/ml, Molecular Probes, Thermo Fisher Scientific, Reinach, Switzerland, Cat. #A-11122, RRID:AB_221569), mouse anti-GFP (diluted 0.1 μg/ml, Molecular Probes, Thermo Fisher Scientific, Reinach, Switzerland, Cat. #A-11120, RRID:AB_221568), and rabbit anti-Iba1 (diluted 1 μg/ml, Wako, Neuss, Germany, Cat. #019–19741, RRID:AB_839504). Primary antibodies were diluted in 0.1M TBS pH 7.3 with 0.1% Triton X-100 and 10% bovine serum and incubated overnight at 4°C. Primary antibody staining was revealed using species-specific fluorophore-conjugated secondary antibodies (Cy3, Alexa Fluor 488 and Alexa Fluor 647, Jackson Immuno Research/Milan Analytica, Rheinfelden, Switzerland). Cy3, Alexa Fluor 488 and Alexa Fluor 647-conjugated secondary antibodies were diluted in 0.1M TRIS pH 8.2 at 4 μg/ml working concentration and incubated for 3 hr at room temperature. To exclude nonspecific labeling or high degrees of autofluorescence in the samples, free-floating coronal sections—encompassing regions of LV-wall adhesions—incubated only with secondary antibodies were used as negative controls. Nuclear counterstaining was performed by incubation with 4′,6-diamidino-2-phenylindole (DAPI, Molecular Probes, LuBioScience, Lucerne, Switzerland) diluted in 0.1M PBS pH 7.4 at 10 μg/ml working concentration for 30 min at room temperature. Between incubation steps, 3 × 5 min thorough washes in 0.1M TBS pH 7.3 were applied. Immunostained sections were mounted on Superfrost Plus slides (Thermo Fisher Scientific, Reinach, Switzerland), air-dried at 37°C for 30 min, and covered with standard thickness (No. 1) 24 × 60 mm cover slips (Gribi AG, Belp, Switzerland) with aqueous nonfluorescent mounting medium (Hydromount by National Diagnostics, Chemie Brunschwig AG, Basel, Switzerland).

2.3 | Characterization of the antibodies and antisera

We confirmed the specificity of the antibodies and antisera used in this study by Western blotting. Brains from adult C57Bl/6 and PV-KO and muscle tissue from PV-eGFP euthanized mice were quickly removed, homogenized and soluble proteins were extracted for Western blotting experiments. Proteins (50 μg for brain and muscle lysates) were separated by sodium dodecyl suflate polyacrylamid geleletrophoresis (SDS-PAGE) (12%). After electrophoresis, the proteins were transferred on nitrocellulose membranes (MS solution, Chemie Brunschwig, Basel, Switzerland). The membranes were then blocked in 5% nonfat milk in TBS-T for 20 min at room temperature and incubated with primary antibodies as listed in Table 1 in 2% nonfat milk in TBS-T overnight at 4°C. Membranes were washed three times in TBS-T and incubated for 1 hr with secondary antibodies: horseradish peroxidase (HRP) conjugated goat anti-rabbit IgG 1:10,000, HRP conjugated goat anti-mouse IgG 1:5,000 (Sigma-Aldrich, Buchs, Switzerland) or HRP conjugated donkey anti-guinea pig IgG 1:5,000 (Jackson Immuno Research/Milan Analytica, Rheinfelden, Switzerland) in TBS-T. Finally, membranes were repeatedly rinsed in TBS and developed using enhanced chemiluminescence (ECL) (Merck Millipore, Schaffhausen, Switzerland). Bands were visualized using FluorChem E (San Jose, CA). Additionally, we confirmed the staining patterns of each antibody and antiserum (Table 1) on coronal brain sections throughout the whole brain by immunofluorescence as described above.

The polyclonal guinea pig PV antiserum was raised against recombinant mouse PV. The polyclonal rabbit PV antiserum was raised against recombinant rat PV. In Western blot, a single band at the molecular weight level of PV (~12 kDa) was detected by both rabbit

and guinea pig anti-PV antibodies in brain extracts form wild-type (WT) animals while no signal was detected in extracts from PV-KO mice (Figure 1a,b). Pure mouse recombinant calretinin and calbindin proteins were used as additional negative controls, and pure mouse recombinant PV protein as positive control (Figure 1a,b). Known amount of pure mouse recombinant PV protein was loaded on the same blot used as reference protein (normalization control). The relative affinity of anti-PV antibodies in each sample ($n = 3$ for PV 25 and

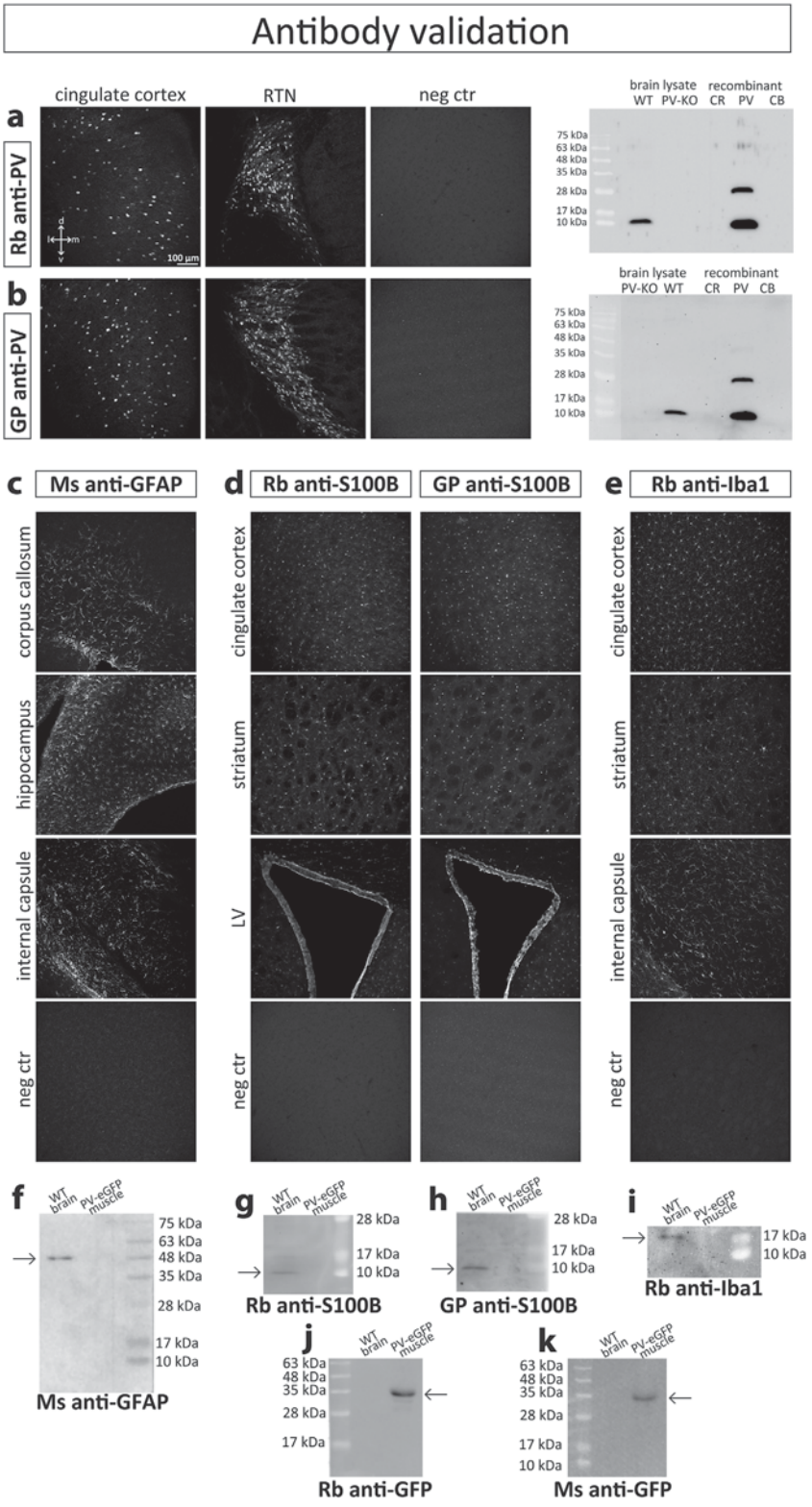

FIGURE 1.

$n = 3$ for GP72) was determined by calculating the ratio of the intensity of the signal for PV to that of the normalization control. Both the rabbit and guinea pig anti-PV antibodies showed similar affinity for the target protein (8.04% ± 3.8 for GP72 and 7.6% ± 3 for PV 25, $p = .885$). Additionally, we calculated the ratios of the intensity of the signal for the recombinant protein. Both anti-PV antibodies showed similar affinity for the pure recombinant PV protein. We also confirmed by immunofluorescence that the staining patterns of both anti-PV antibodies were identical in different brain areas regarding cellular morphology and distribution and consistent with that of PV-interneurons (Figure 1a,b) as demonstrated previously (Filice, Vorckel, Sungur, Wohr, & Schwaller, 2016; Xu, Roby, & Callaway, 2010). These results confirm the specificity of the anti-PV antibodies.

The monoclonal anti-GFAP antibody was raised against purified pig spinal cord GFAP. We tested the antibody by immunofluorescence on murine coronal brain sections and confirmed that the pattern of staining regarding cellular morphology and distribution in the brain was consistent with that of astrocytes (Figure 1c) as demonstrated in previous studies (Sofroniew & Vinters, 2010). This antibody was shown to label astrocytes in previous studies as well (Brai et al., 2014; Szabolcsi & Celio, 2015). In Western blot, the antibody detected a single band at about 50 kDa—corresponding to the major isoform of GFAP—in murine brain protein extract (Figure 1f), whereas no signal was detected in muscle protein extract (negative control).

The polyclonal rabbit S100B antiserum was raised against purified bovine brain S100B. We confirmed that the staining pattern throughout the brain regarding cellular morphology and distribution corresponds to astrocytes and ependymal cells (Figure 1d) as demonstrated in previous studies (Raponi et al., 2007; Spassky et al., 2005). In Western blot, the antiserum detected a prominent band at about 10 kDa—corresponding to the expected molecular weight of S100B—in mouse brain protein extract, whereas no signal was detected in muscle protein extract (Figure 1g). The S100B antiserum was used to label ependymal cells in murine brain sections and organotypic slice cultures in our previous study (Szabolcsi & Celio, 2015). Previous studies showed that in Western blot analysis of gerbil brain lysate, the S100B antiserum recognized the expected band at about 10 kDa (Ford, Grothe, & Klug, 2009).

The polyclonal guinea pig S100B antiserum was raised against recombinant full length rat S100B. We tested the specificity of the antiserum by comparing the staining pattern with that of the polyclonal rabbit S100B antiserum on coronal murine brain sections throughout the entire brain. We confirmed that the staining patterns were identical (Figure 1d). In Western blot, the antiserum detected a prominent band at the expected molecular weight 10 kDa in murine brain protein extract, while no signal was detected in muscle protein extract (Figure 1h).

The purified polyclonal rabbit Iba1 antiserum was raised against a synthetic peptide corresponding to the C-terminus of Iba1. We confirmed by immunofluorescence that the staining pattern of the Iba1 antiserum in the brain regarding cell morphology and distribution is consistent with that of microglial cells (Figure 1e) as demonstrated in previous studies (Ito et al., 1998). In Western blot, the antiserum detected the expected band at about 17 kDa corresponding to the molecular weight of Iba1 (Figure 1i). This Iba1 antibody was shown to label murine microglial cells in previous studies as well (Bosco, Steele, & Vetter, 2011; Petkau et al., 2010).

The polyclonal rabbit GFP antiserum was raised against GFP protein isolated from the jellyfish *Aequorea victoria*. We previously confirmed the immunofluorescence specificity by comparing the staining pattern with the eGFP-expression pattern in Foxj1-eGFP and PV-KO-eGFP organotypic hippocampal slice cultures (Szabolcsi & Celio, 2015). In Western blot, the antibody detected a single band at about 30 kDa in PV-eGFP muscle protein extract corresponding to the expected molecular weight of GFP, while no signal was detected in the WT brain

FIGURE 1 Characterization of the antibodies and antisera. We confirmed the specificity of the antibodies and antisera used in this study by Western blotting, respectively by analyzing the immunofluorescence staining patterns. Confocal z-stack overprojections in the regions of the cingulate cortex and reticular thalamic nucleus (RTN) depict PV-immunopositive neurons stained with rabbit anti-PV (PV 25, Swant) (a) and with guinea pig anti-PV (GP72, Swant) (b) antibodies. The staining patterns of the two anti-PV antibodies are comparable. Whole brain protein extracts from adult C57Bl/6 and PV-KO mice were separated by SDS-PAGE and transferred on nitrocellulose membranes. After blocking, the membranes were incubated with rabbit anti-PV (a) and guinea pig anti-PV (b) antibodies. Pure recombinant calretinin (CR) and calbindin (CB) proteins were used as additional negative controls, and pure recombinant parvalbumin (PV) protein as positive control. A single band at the expected molecular weight of PV (~12 kDa) was detected by both antibodies in brain extracts form wild-type (WT) animals, while no signal was detected in extracts from PV-KO mice (a, b). Pure recombinant PV tends to form dimers in solution, which were also detected by both antibodies at about 24 kDa in addition to the expected 12 kDa signal (a, b). Confocal z-stack overprojections depict GFAP-immunostained astrocytes in the corpus callosum, hippocampus and internal capsule (c), S100B-immunostained astrocytes in the cingulate cortex and striatum, respectively ependymal cells in the lateral ventricle (LV) walls (d), and Iba1-immunostained microglia in the cingulate cortex, striatum, and internal capsule (e). Coronal sections incubated with secondary antibodies without previous incubation with primary antibodies were used as negative controls. The staining pattern of the mouse anti-GFAP antibody (Novus Biologicals) is consistent with that of astrocytes (c). The rabbit anti-S100B (Swant) and the guinea pig anti-S100B (Synaptic Systems) staining patterns appear comparable (d). The Iba1-immunostaining pattern is consistent with that of microglia (e). In Western blot analysis, the mouse anti-GFAP detects the expected band at about 50 kDa in the murine brain and gives no signal in the muscle protein extract (f). The rabbit anti-S100B detects a prominent band at about 10 kDa in the murine brain protein extract, while no signal is detected in muscle protein extract (g). Similarly, the guinea pig anti-S100B detects a prominent band at about 10 kDa in the murine brain protein extract, and no signal in the muscle protein extract (h). The anti-Iba1 detects the expected band at about 17 kDa in the murine brain lysate, with no signal detected in the muscle extract (i). Both the rabbit anti-GFP (j) and mouse anti-GFP (k) antibodies recognize the expected band about 30 kDa in the PV-eGFP muscle protein extract, while they detect no signal in the WT brain protein extracts. GP = guinea pig; Ms = mouse; Rb = rabbit

protein extract (Figure 1j). In previous studies, the antibody was shown to detect a single band in Western blot analysis of whole-cell lysates from GFP-transfected normal human epidermal keratinocytes (NHEK) cells, and was negative in untransfected cells (Hiroyasu et al., 2013).

The monoclonal anti-GFP antibody was raised against GFP protein isolated from the jellyfish *A. victoria*. We tested the immunofluorescence specificity by confirming that the staining pattern coincided with the eGFP-expression in Foxj1-eGFP, respectively in PV-KO-eGFP organotypic hippocampal slice cultures (Szabolcsi & Celio, 2015) and in coronal brain sections derived from Glycine transporter 2 (GlyT2)-eGFP mice (Szabolcsi, Albisetti, & Celio, 2017). In Western blot, the antibody detected a single band at about 30 kDa in PV-eGFP muscle protein extract corresponding to the expected molecular weight, while no signal was detected in the WT brain protein extract (Figure 1k).

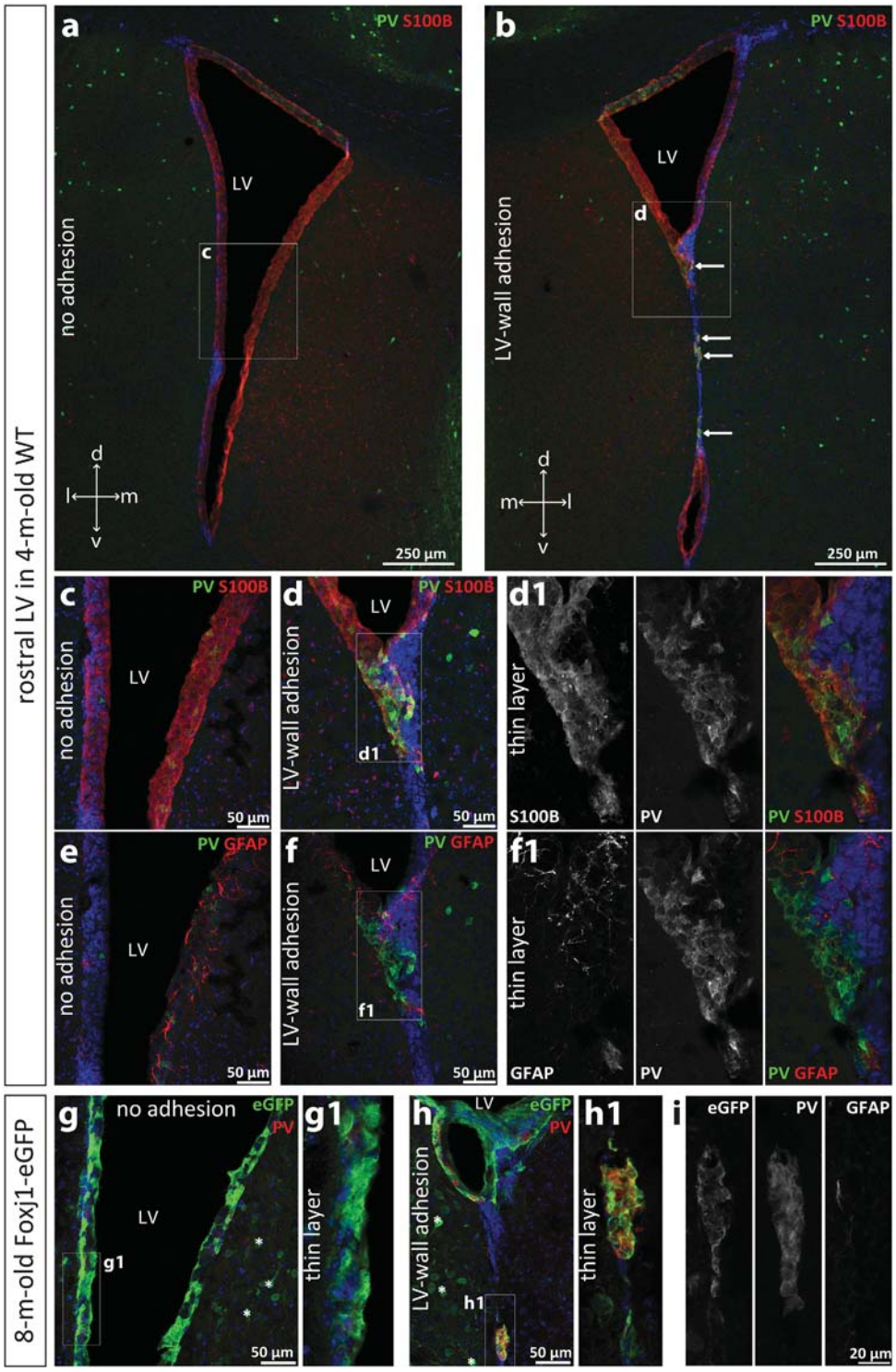

FIGURE 2.

2.4 | Stereological volume estimation

Forty-micrometer-thick coronal sections of C57BL/6 ($n = 13$) and PV-KO ($n = 18$) mice were collected consecutively, maintaining a rostrocaudal order. Sections encompassing the region of the rostral LVs were immunostained with anti-S100B, anti-PV and anti-GFAP antibodies, and counterstained with DAPI. A systematic random sampling (SRS) series was generated by randomly choosing section number 1 out of the 3 consecutive sections following section "zero." Section "zero" was defined as the first section where the LVs rostrally appear, usually corresponding approximately to Bregma level +1.5 mm. Every 6th section starting from section no. 1 were mounted until ca. Bregma level 0.0 mm, thus resulting in a series of six coronal sections encompassing approximately a 1.5 mm length along the sagittal axis of the rostral portion of the LVs. The series of sections were analyzed with a stereology workstation consisting of a Zeiss Axioplan microscope (Carl Zeiss AG, Feldbach, Switzerland) equipped with Stereo Investigator software (MBF Bioscience, Magdeburg, Germany, RRID:SCR_002526). The volume of the LVs and of the LV-wall adhesions were determined according to the Cavalieri principle (Gundersen & Jensen, 1987) applying the Cavalieri Estimator Probe. A grid spacing of 50 μm was used for the volume estimation of the LV volume, respectively a grid spacing of 20 μm for the volume estimation of the LV-wall adhesions.

2.5 | In vivo stereotactic lesion of the LV walls

Adult (4- to 5-month-old) Foxj1-eGFP mice ($n = 3$) were anesthetized with a solution of Ketamine/Xylazine (100 mg/kg and 10 mg/kg body weight, respectively) dissolved in 0.9% NaCl solution and their heads were restrained in a stereotactic apparatus (Kopf Instruments, Tujunga, CA). The lesion was carried out unilaterally over the left LV with a 1-mm-long-blade. The stereotactic coordinates of the lesion were mediolaterally +2.5 mm, rostrocaudally between Bregma −1.0 and −2.0 mm, depth from skull surface 3 mm. Lesioned mice were transcardially perfused with a 4% PFA solution in 0.1 M PBS (pH 7.4) 1 week after the injury, the brains were post-fixed overnight at 4°C, transferred to cryoprotectant solution (18% saccharose) and processed for cutting 40-μm-thick-sections with a freezing microtome (Frigomobil, Reichert-Jung, Vienna, Austria). Immunofluorescence on free-floating sections was performed with anti-GFP, anti-PV, and anti-GFAP antibodies.

2.6 | Imaging

Coronal brain sections were imaged by a Nanozoomer 2.0-HT digital slide scanner (Hamamatsu Photonics France, Massy, France), a Leica TCS SP5 confocal laser scanning microscope, and a Leica DM 6000B fluorescence microscope (Leica, Germany). Confocal z-stacks were superposed in maximum intensity projections using ImageJ (Fiji, RRID: SCR_002285), or are presented as thin layer reconstructions. Thin layer reconstructions were performed by maximum intensity projection of only few z-planes by ImageJ, resulting in 3–5 μm thin optical sections. The entire image sequences of raw confocal z-stacks from Figures 2–3, and 7, respectively of the negative controls are available as an open access data set on Zenodo (http://doi.org/10.5281/zenodo.437943). Image post-processing was limited to contrast adjustment only and was done by ImageJ.

2.7 | Image acquisition by confocal microscopy

The Leica TCS SP5 confocal laser scanning microscope system used for fluorescence intensity measurement was equipped with an inverted Leica DMI 6000 stand with motorized stage, conventional galvo scanner, four lasers: diode laser (405 nm), Argon laser (458, 477, 488, 496, and 514 nm), diode pumped solid state laser (561 nm), and Helium-Neon laser (HeNe, 633 nm), Acousto-Optical Beam Splitter as tunable dichroic for all lasers, and three photomultiplier tube detectors with spectral detection. Regular instrument calibration and adjustment was performed according to the guidelines of the manufacturer. Confocal z-stacks were acquired with a Leica HC PL APO CS2 40.0x 1.30 OIL UV objective (numeric aperture: 1.30, magnification: 40.0×, corrections CS, UV, apochromatic (APO), refraction index: 1.52), pinhole was set to 68.3 μm (airy 1.05), z-step size to 0.42 μm. No frame or line accumulation, respectively averaging was used. The parameters of image acquisition (laser and acousto-optic tunable filter (AOTF) intensity, gain,

FIGURE 2 Nonaged (4-month-old) C57BL/6 mice exhibit unilateral ventricle stenosis and PV-immunopositive ependymal cells in the adhering ependymal layers. Confocal laser z-stack overprojections depict the nonadhering LV walls (a) and the adhering ones on the contralateral side (b). Immunofluorescence for S100B revealed a uniform staining of the ependymal layers in the nonadhering LV walls (a), whereas a continuous S100B-stained ependyma was lacking in the LV-wall adhesion (b). Instead, patches of S100B-positive ependymal cells could be observed in the adhesion zone (b, arrows). PV-immunostaining was found in S100B-immunopositive ependymal cells (d), whereas it was virtually absent from the normal, nonadhering LV walls (c). Approximately 5-μm-thick thin layer reconstruction of few z-planes shows co-expression of S100B and PV-immunofluorescence in the same cells in the LV-wall adhesions (d1). GFAP-immunostaining on the same sections revealed several GFAP-stained astrocytic processes intermingled in the PV+ ependymal-cell clusters of the LV-wall adhesions (f), as well as in the normal, nonadhering ependymal layer on the contralateral side (e). In thin layer reconstruction of few z-planes, no co-labeling between GFAP- and PV-staining was observed (f1). We examined the LV walls of 8-month-old Foxj1-eGFP mice, which display transgenic eGFP-expression in ependymal cells. Confocal z-stack overprojections of nonadhering LV walls depict eGFP-stained ependymal layers with virtually absent PV-immunoreactivity (g, g1), whereas adhered LV walls display Foxj1-eGFP+/PV+ cell islands (h). Thin layer reconstruction of few z-planes (approximately 4 μm thick) demonstrates that PV and eGFP are co-expressed in the same cells (h1). Confocal z-stack maximum overprojection of GFAP-immunostaining shows GFAP-immunopositive processes infiltrated in the adhesion site, with no co-expression of GFAP and Foxj1-eGFP or PV in the LV-wall adhesions cells (i). The scattered eGFP-positive cells medial to the LV walls (g, h, asterisks) might represent ectopic eGFP-expression. d = dorsal; l = lateral; LV = lateral ventricle; m = medial; v = ventral

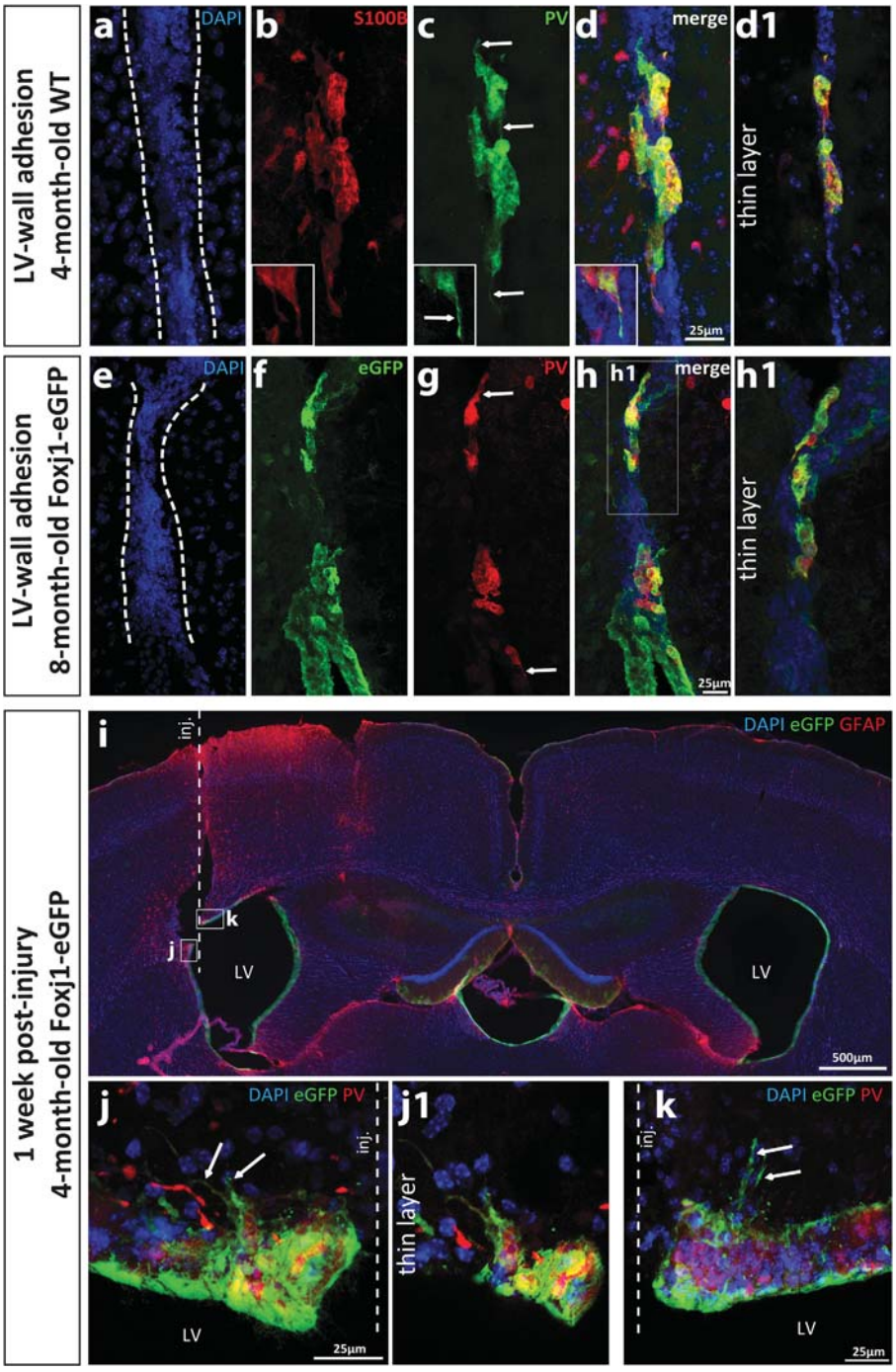

FIGURE 3 PV-immunopositive ependymal cells in the LV-wall adhesions acquire reactive phenotype, similarly to injury-reactive ependymal cells. Confocal laser z-stack overprojections of 4-month-old C57BL/6 mice display PV- and S100B-co-stained ependymal cells in the region of the LV-wall adhesions (a–d, adhered LV walls marked by dashed lines). Thin layer reconstruction of few z-planes is shown in (d1). The insets in (b–d) depict an example from another animal in a corresponding region of LV-wall adhesion. Confocal laser z-stack overprojection of 8-month-old Foxj1-eGFP mice depicts eGFP+/PV+ cells in the LV-wall adhesion (e–h, adhered LV walls marked by dashed lines), magnified thin layer reconstruction image is shown in (h1). Some of the PV-expressing ependymal cells possess elongated cellular processes that extend into the adhesion (c, g, arrows). This cell morphology suggests a reactive phenotype, and resembles that observed in reactive post-injury ependymal cells (i–k). Unilateral in vivo stab-wound (marked by a dashed line) over the cortex and LV wall was performed in Foxj1-eGFP mice (i). One week following lesion, GFAP-immunostaining depicts reactive astrocytes around the stab-wound in the parenchyma, while GFP-staining reveals a lesioned, interrupted ependymal layer (i). Confocal z-stack overprojections of the ependymal layer adjacent to the stab-wound injury display several reactive eGFP+ cells with long basal processes extending into the parenchyma, approximately perpendicularly to the ependymal layer (j, k, arrows). Some of these Foxj1-eGFP+ ependymal cell processes co-express PV, as shown in thin layer (of approximately 3 μm thickness) reconstruction image in (j1). Cell morphological features seen in (j) and (k) are similar to those of PV-immunopositive ependymal cells found in the LV-wall adhesions (a–h). inj. = stab-wound injury; LV = lateral ventricle

offset, etc.) were set to maximize signal-to-noise ratio and to avoid over- or underexposure throughout the entire z-volume of the samples, following well-established guidelines (Waters, 2009). Double- or triple-stained sections were imaged at 8-bit color depth, 1,024 × 1,024 pixel format and 200 Hz scan speed as z-stacks using sequential scanning mode, the emission bandwidths being 418–487 nm (laser intensity 30%, active gain 498 V, offset −1) for DAPI, 503–543 nm (AOTF intensity 15%, active gain 844 V, offset −6) for Alexa Fluor 488-conjugated fluorescent secondary antibodies, 572–630 nm (AOTF intensity 15%, active gain 497 V, offset −2) for Cy3-conjugated fluorescent secondary antibodies, 650–729 nm (AOTF intensity 15%, active gain 745 V, offset −3) for Alexa Fluor 647-conjugated secondary antibodies.

2.8 | Fluorescence intensity quantification

Maximum intensity projections of confocal z-stacks acquired from coronal brain sections in the regions encompassing the rostral LVs were used to measure the fluorescence intensity of the PV- and GFAP-immunostaining in the ventricular and periventricular area of the LV walls. Briefly, SRS series of coronal sections were prepared as described above from C57BL/6 adult mice ($n = 8$, 4- to 15-month-old) and the regions encompassing the LVs were imaged by confocal z-stack acquisition maintaining the same settings of gain, AOTF intensity and offset throughout the analysis of all the animals. Confocal z-stack image series were superposed in maximum intensity projections by ImageJ. The overprojection images were merged together applying the "Pairwise stitching" plugin in ImageJ to allow the visualization of the entire dorsoventral extent of the LVs. The areas lying outside the periventricular region were manually cleared to exclude intensity measurement of PV- and GFAP immunostained regions outside the regions of interest (ROIs). Briefly, the workflow of the fluorescence intensity measurement was performed as follows. The merged, cleared 8-bit images of PV-, respectively GFAP-immunostaining of both LVs from six coronal sections of all animals were added into one image sequence, thus creating 12 images per animal. The periventricular PV- and GFAP-immunofluorescence intensity was analyzed separately. The particle analysis by ImageJ requires 8-bit greyscale images with 256 intensity graduations which can be assigned to a pixel (pixel intensity 0 corresponding to no signal, while 255 to maximal signal). Therefore, a threshold range was set to tell the objects of interest apart from the background by the "Adjust threshold" command in ImageJ. After testing several thresholding settings, we defined the optimal threshold to be 70–255 for the entire image sequence, thus excluding the analysis of all the pixels whose intensity value was below 70. We then subjected the image sequence to the "Analyze particles" plugin, by applying no particle size filter or circularity filter. Area, mean, minimal and maximal gray value, standard deviation, area fraction, and integrated density were measured and summarized for each image, and exported as Excel tables. IntDen is the product of the area and the mean gray value, reflecting the total area and fluorescence intensity of PV-, respectively GFAP-immunofluorescence of each image of the LVs. The mean IntDen corresponds to the average IntDen of the periventricular regions of six coronal sections after subtraction of the IntDen values of the negative controls (28.17 ± 12.4 for PV and 33.87 ± 4.85 for GFAP) from each value. Negative control sections were incubated with the secondary antibodies only, and the regions of the LV-wall adhesions were processed for confocal imaging as described above, followed by the fluorescence intensity measurement workflow described here.

In another set of experiments, Iba1-immunostained coronal sections of WT ($n = 6$) and PV-KO ($n = 6$) mice of different ages ranging from 6- to 15-month-old were imaged by a Leica DM 6000B fluorescent microscope. In the regions encompassing the LV wall adhesions, at least four 40-μm-thick-sections—spaced 160 μm from each other—per mouse were imaged, maintaining the same settings of image acquisition for all the animals. Several ROIs with an area of 268.57 μm × 307.62 μm were defined in the images; in the regions of the LV-wall adhesions and in the striatum adjacent to the LV walls in the same section serving as control Iba1-staining. All the images were added into a single image sequence, which was subjected to the fluorescence intensity measurement workflow described above. We defined the optimal threshold to be 50–255 for the entire image sequence, and subjected it to the "Analyze particles" plugin applying a particle size filter $\geq 15\ \mu m^2$. Area, mean, minimal and maximal gray value, standard deviation, area fraction, and IntDen were measured and summarized for each image in the image sequence, and exported as Excel tables. The mean IntDen values of the Iba1-immunofluorescence intensity of the LV-wall adhesions, respectively the striatum represent the average of the analyzed sections. The mean IntDen values in the LV-wall adhesions were compared with the values of the striatum as control.

2.9 | Statistics

To compare the data sets, statistical strength was analyzed by GraphPad Prism 7 (RRID:SCR_002798) using ordinary one-way ANOVA with Sidak's multiple comparisons test upon verification of the Gaussian distribution of the data, and Kruskal-Wallis test with Dunn's multiple comparisons test when Gaussian distribution of the data failed. Curves were analyzed by linear regression analysis in GraphPad Prism 7 where goodness of fit (R square) and the significance of the slope's deviation from zero were calculated.

3 | RESULTS

3.1 | PV-expressing ependymal cells of reactive phenotype can be found in LV-wall adhesions of nonaged WT mice

In young adult (4-month-old) C57BL/6 mice ($n = 5$), we found the lateral and medial walls of the rostral portion of the LV to adhere to each other, resulting in unilateral or bilateral ventricle stenosis. We observed that the nonadhering LV walls displayed an uninterrupted, healthy ependymal layer visualized by the ependymal-cell marker S100B with virtually absent PV-expression (Figure 2a,c). However, in the regions of LV-wall adhesion, the ventricle walls partially lacked an intact ependymal layer (Figure 2b). Instead, patches of S100B-stained ependymal-cell islands could be observed in the adhesions (Figure 2b, arrows), which also displayed PV-immunoreactivity in addition to S100B-

expression (Figure 2d). We also examined the single z-planes of the confocal z-stacks for co-expression, and we found S100B+/PV+ cells in the adhered LV walls (Figure 2d1, thin layer reconstruction). Large portions of the adhered LV walls were devoid of an S100B+ ependymal layer, which is in line with previous observations that described the loss of ependymal cells in the LV-wall fusions in aging mice (Shook et al., 2012). We also examined if ependymal cells in LV-wall adhesions co-expressed the astrocyte marker GFAP, similarly to reactive ependymal cells following mechanical injury (Szabolcsi & Celio, 2015) and stroke (Young et al., 2013). We found GFAP-immunopositive processes to infiltrate the adhesion site and to intermingle with the PV+ cells (Figure 2f); however, upon examination of single confocal z-planes throughout the adhesion site and thin layer reconstructions, we did not detect co-expression of GFAP and PV in the same cells (Figure 2f1). The nonadhering LV walls also displayed numerous strongly stained GFAP-positive processes in the ependymal layer (Figure 2e). The dense periventricular GFAP-immunostained astrocytic processes reflect ventricular astrogliosis (hereafter: ventricular gliosis) which is associated with ventriculomegaly in the human and murine brain (Shook et al., 2013). By visual observation, ventricular gliosis represented by GFAP-immunostaining did not appear to be more pronounced in the LV-wall adhesion site than in the nonadhered LVs (Figure 2e,f).

Given that S100B labels astrocytes in addition to ependymal cells (Cocchia, 1981), we used an additional approach to ascertain that PV-expressing cells in the LV-wall adhesions were indeed of ependymal origin. In a second set of experiment, we examined the LV walls of 8-month-old Foxj1-eGFP mice ($n = 5$). The forkhead transcription factor FoxJ1 regulates ciliogenesis in mice and it is required for the differentiation of radial glial cells into ependymal cells. Foxj1-driven eGFP-expression in the brain is restricted to ependymal cells (see also Figure 3i) and to a small subset of Foxj1-positive astrocytes derived from the ventricular zone (Jacquet et al., 2009; Ostrowski et al., 2003). PV- and GFP-immunostained coronal sections displayed strongly GFP-stained ependymal layers in the nonadhering LV walls, with virtually absent PV-immunoreactivity (Figure 2g,g1). In the LV-wall adhesions, islands of Foxj1-eGFP+/PV+ cells were present (Figure 2h). PV and eGFP were co-expressed in the same cells, as shown by thin layer reconstruction of the confocal z-stacks (Figure 2h1). Although GFAP-immunopositive processes infiltrated the adhesion site, Foxj1-eGFP expressing cells in the LV-wall adhesions did not co-express GFAP (Figure 3i). Therefore, we assume that Foxj1-eGFP+/PV+ cells in the LV-wall adhesions were of ependymal origin. In Foxj1-eGFP mice, in addition to the extensive eGFP-expression in the ependymal layer of the ventricular zone, we also observed scattered eGFP-expressing cells medially from the LV walls (Figure 2g,h, asterisks), which did not co-express PV or GFAP. These scattered Foxj1-eGFP positive cells are present in a region corresponding to the lateral septal nucleus and might represent an ectopic eGFP-expression in this mouse line given that the cells do not co-express astrocyte markers (GFAP or S100B, data not shown). The entire image sequences of the confocal z-stacks from Figures 2–3, and 7, respectively of the negative controls (not shown) have been deposited as an open access data set on Zenodo (http://doi.org/10.5281/zenodo.437943).

3.2 | PV-expressing ependymal cells in LV-wall adhesions acquire a reactive phenotype

When we examined the morphology of PV-stained ependymal cells of the LV-wall adhesions (Figure 3a–d), we observed elongated, bipolar cell shape with long, thin cellular processes (Figure 3c, arrows), which co-expressed the ependymal-cell marker S100B (Figure 3d). We observed similar cell morphology when we analyzed the LV-wall adhesions of Foxj1-eGFP mice (Figure 3e–h). Many of the Foxj1-eGFP expressing cells in the LV-wall adhesions co-expressed PV (Figure 3h1), and some of them displayed elongated cell shape and long cellular processes (Figure 3g, arrows). Normally, ependymal cells are characterized by a cuboidal to columnar shape, apical-basal polarity, and planar cell polarity typical of epithelial-like cells (Del Bigio, 2010; Mirzadeh, Han, Soriano-Navarro, Garcia-Verdugo, & Alvarez-Buylla, 2010). The morphological features we observed in PV-expressing ependymal cells in LV-wall adhesions resemble that of a reactive phenotype seen following lesion of the ependymal layer (Szabolcsi & Celio, 2015) or stroke (Young et al., 2013). In an in vivo model of penetrating brain injury, in which we inflicted a stab-wound lesion onto the dorsal LV wall in a more caudal portion of the LVs in adult Foxj1-eGFP mice (Figure 3i), we found injury-reactive Foxj1-eGFP+ ependymal cells adjacent to the lesion to extend long processes characteristic of reactive phenotype (Figure 3j,k). Numerous injury-reactive ependymal cells also co-expressed PV (Figure 3j,j1), as we described earlier (Szabolcsi & Celio, 2015). When studying the direction in which ependymal-cell processes found in the LV-wall adhesions extended, we observed that they stretched out parallel to the former ventricle surface, along the dorsoventral axis of the adhesion (Figure 3c,g, arrows), whereas post-injury ependymal-cell processes extended basally (Figure 3j,k). One could as well assume that ependymal cells in the adhering LV walls alter their position in the ependymal layer or even lose their cell polarity completely, in addition to acquiring a reactive phenotype. This could be explained if we presume a disintegration of the previously normal ependymal layers caused by adhesions of the opposite LV walls, which might ultimately lead to the transposal of the basal processes along the dorsoventral axis.

3.3 | The volume of LV-wall adhesion shows reciprocal correlation to the volume of the rostral LV

Next, we aimed to quantify the grade of ventricle stenosis in WT, respectively in PV-KO mice. As LV-wall adhesions affect the rostral portion of the LV, we analyzed the region approximately between Bregma levels +1.5 and 0 mm, corresponding to the rostral part of the LV in the murine brain. We used stereological volume estimation to measure the volumes of the LV-wall adhesions and the LVs in adult (6- to 15-month-old) PV-KO ($n = 18$, both sexes) and WT mice ($n = 13$, both sexes). We found that the volume of the LV-wall adhesion showed a strong reciprocal correlation to the LV volume both in WT (Figure 4a) and PV-KO mice (Figure 4b). Based on this finding, we deduced that the volume of the LV-wall adhesion (hereafter: adhesion volume) reflects well on the adhesion extent, therefore on the grade of

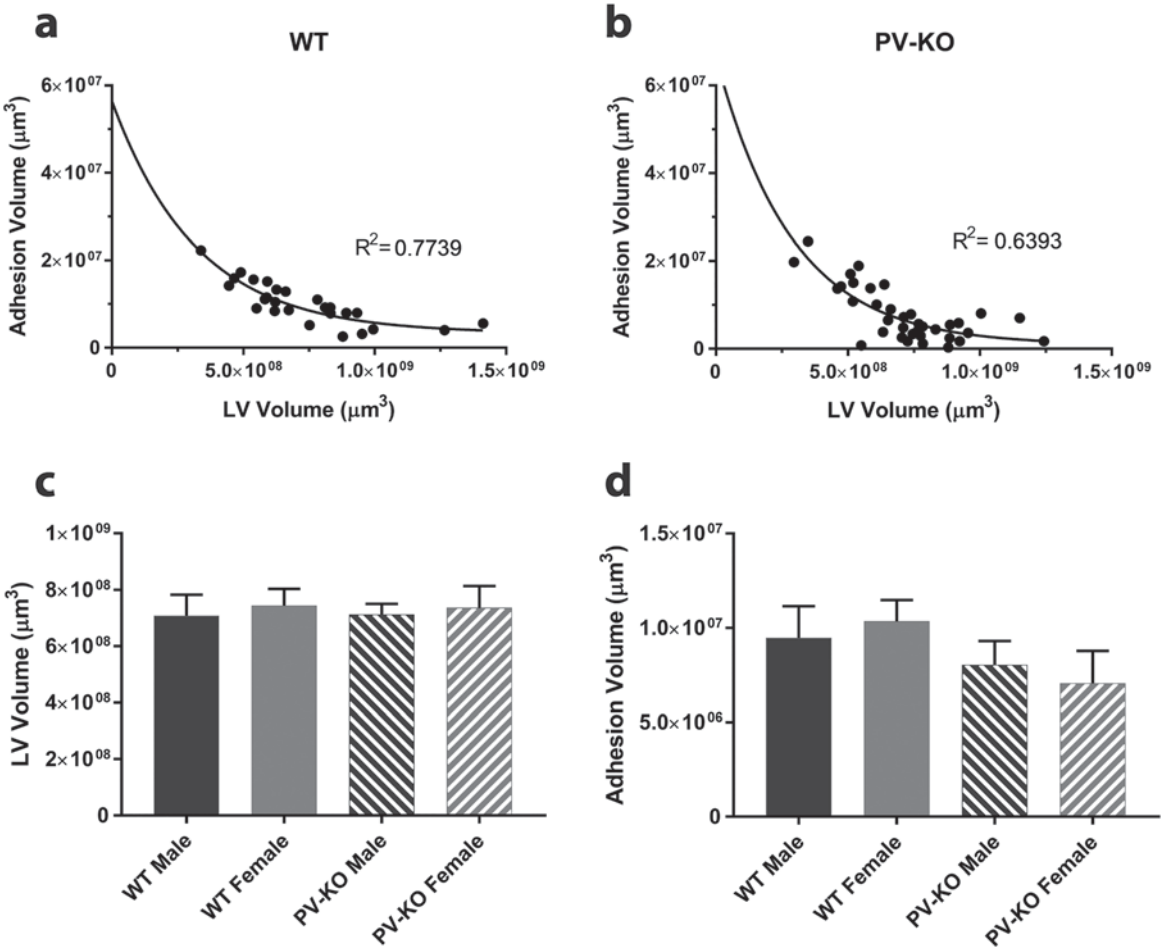

FIGURE 4 LV-wall adhesion volume is reciprocally correlated to the rostral LV volume in both WT and PV-KO mice. The volume of the LV-wall adhesions and the LVs in the rostral portion of the brain (approximately Bregma levels +1.5 to 0 mm) was quantified with stereological methods in adult (6- to 15-month-old) PV-KO ($n = 18$) and WT mice ($n = 13$). LV-wall adhesion volume is in reciprocal correlation with the LV volume in both WT ($R^2 = 0.7739$, a) and PV-KO mice ($R^2 = 0.6393$, b). LV-wall adhesion volume therefore reflects well on the grade of ventricle stenosis. We compared the LV volume and adhesion volume between male and female mice. The LV volume values do not differ significantly between PV-KO and WT males, between PV-KO and WT females, or between males and females in either PV-KO or WT mice (c). Similarly, no significant differences were found regarding adhesion volume (d). Statistical analyses between the groups were performed by one-way ANOVA. Error bars show the standard error of the mean (SEM)

ventricle stenosis. We also examined if there was any difference regarding the values of measured parameters between female and male PV-KO and WT mice. We found no differences between PV-KO and WT males or between PV-KO and WT females regarding the rostral LV volume (Figure 4c) or the adhesion volume (Figure 4d). Therefore, we used mice of both sexes throughout the study.

3.4 | PV-immunofluorescence intensity in the LV walls correlates to the adhesion volume but not to the LV volume in <10-month-old mice, whereas periventricular GFAP-immunofluorescence intensity shows no correlation

Owing to the dense organization of the cell nuclei in the ependymal layer and the characteristics of GFAP-staining that labels the cellular processes and not the cell bodies, we faced difficulty to count PV- and GFAP-immunopositive cells around the LV walls. Therefore, we decided to quantify the intensity of immunofluorescence on confocal laser micrograph z-stack overprojections after manually subtracting the areas outside the periventricular region. We quantified the PV- and GFAP-immunofluorescence intensity in the region of the rostral LV walls and compared the values to the adhesion volume—reflecting adhesion extent—and to the rostral LV volume in C57BL/6 mice ($n = 8$). We used the IntDen (ImageJ) as the parameter that reflects the fluorescence intensity at the best, as it is the product of the area and the mean gray value. Cleared confocal z-stack overprojection micrographs encompassing the rostral portions of the LVs were processed for particle analysis following threshold adjustment by ImageJ, and the IntDen values were presented as means per ventricle upon averaging and subtraction of the IntDen values of the negative controls. We plotted the fluorescence intensity values relative to adhesion volume and to LV volume, and found that in mice younger than 10-month-old,

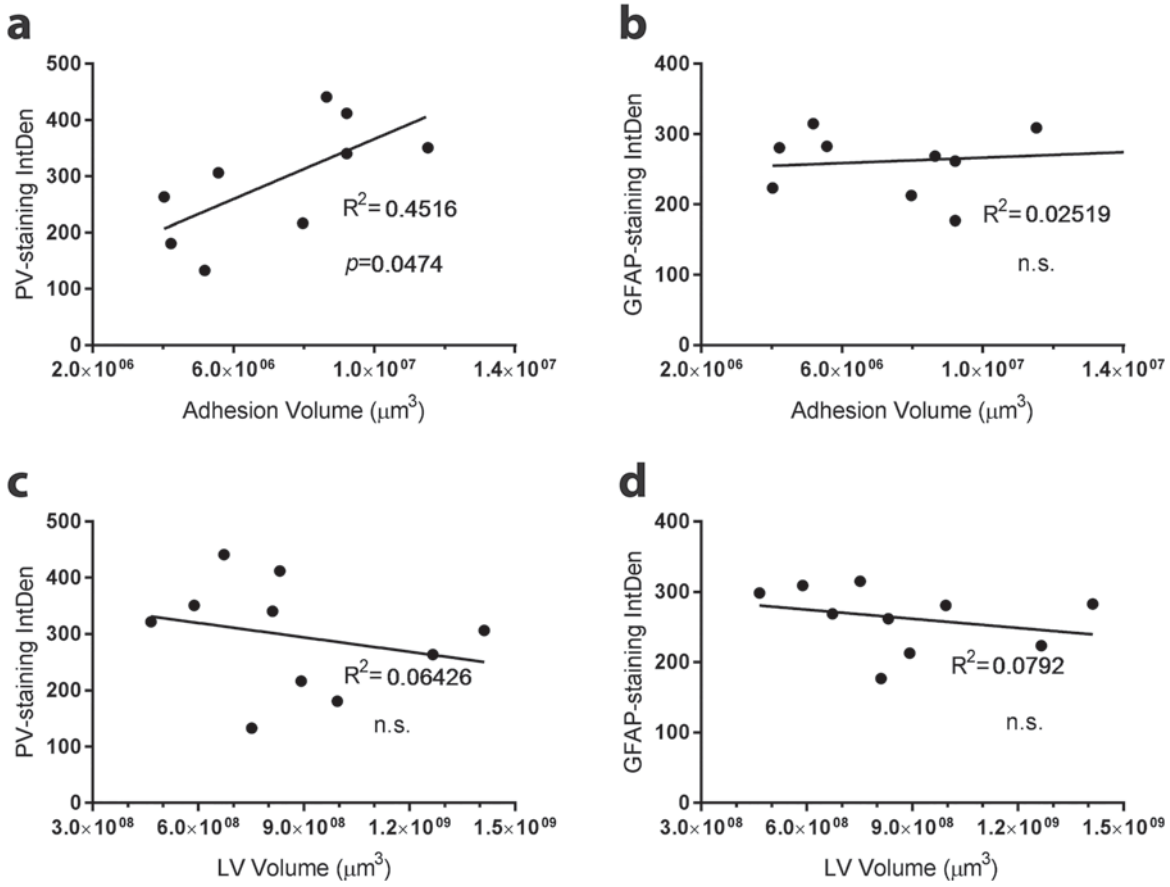

FIGURE 5 Periventricular PV-immunofluorescence is positively correlated to LV-wall adhesion volume and not to LV volume in mice younger than 10-month-old, whereas no correlation applies for periventricular GFAP-immunofluorescence. Periventricular PV- and GFAP-immunofluorescence intensity was quantified in confocal z-stack overprojection images of coronal sections of C57BL/6 mice (aged between 6 and 15 months, $n = 8$) upon excluding regions outside the periventricular area. Following threshold adjustment and particle analysis by ImageJ, the integrated density (IntDen, product of area and mean gray value) of PV- and GFAP-immunofluorescence images was calculated and averaged following subtraction of the IntDen values of the negative controls. The mean IntDen was plotted relative to the adhesion volume and to the LV volume. In nonaged mice (<10-month-old, $n = 5$), PV-immunofluorescence showed positive linear correlation to the adhesion volume ($R^2 = 0.4516$, $p = .0474$, one outlier removed) (a). No significant correlation applied between PV-immunofluorescence and LV volume (b), or between GFAP-immunofluorescence and adhesion volume (c), respectively LV volume (d). In older mice (>10 month-old, $n = 3$), none of the above-mentioned parameters were found to be correlated

PV-immunofluorescence was positively correlated to the volume of the LV-wall adhesion. The correlation between IntDen of the PV-immunofluorescence and adhesion volume was found to be significantly linear ($R^2 = 0.4516$, $p = .0474$, $n = 5$) (Figure 5a). In the same group of animals, no correlation between periventricular PV-immunofluorescence and LV volume was found (Figure 5c), furthermore, GFAP-immunofluorescence intensity reflected by IntDen mean correlated neither to the adhesion volume (Figure 5b) nor to the LV volume (Figure 5d). In older mice (>10-month-old, $n = 3$), we found no correlation between the above-mentioned parameters (data not shown). These findings suggest that the presence of PV+ ependymal cells in the adhering LV walls is linked to the stenosis grade at the early stages of the course of LV-wall fusion. In aged mice, in which permanent LV-wall fusions are already formed, no such correlation applies. On the other hand, ventricular gliosis reflected by periventricular GFAP-staining seems to be unrelated to the extent of LV-wall adhesion and ventricle stenosis grade in all the examined age groups. This is in line with the observation that ventricular gliosis is associated with ventriculomegaly, whereas no such link to ventricle stenosis has been described (Shook et al., 2013). Based on these results, we presume that the early presence of PV+ ependymal cells and not ventricular gliosis is associated with the formation of LV-wall fusions, which then leads to ventricle stenosis and SVZ-decline throughout aging.

3.5 | S100B+/PV+ ependymal cells diminish in LV-wall adhesions in aging mice, whereas periventricular gliosis changes spatial distribution

Based on these results, we raised the question whether PV-immunoreactivity in LV-wall adhesion ependymal cells declines in older mice. Therefore, we analyzed the LVs of 4-month-old ($n = 3$), 8-month-old ($n = 5$), and 15-month-old ($n = 3$) WT mice. Co-immunostaining for S100B, GFAP and PV showed S100B+/PV+ ependymal cell clusters in the LV-wall adhesions of 4-month-old (Figure 6a, arrows) and 8-

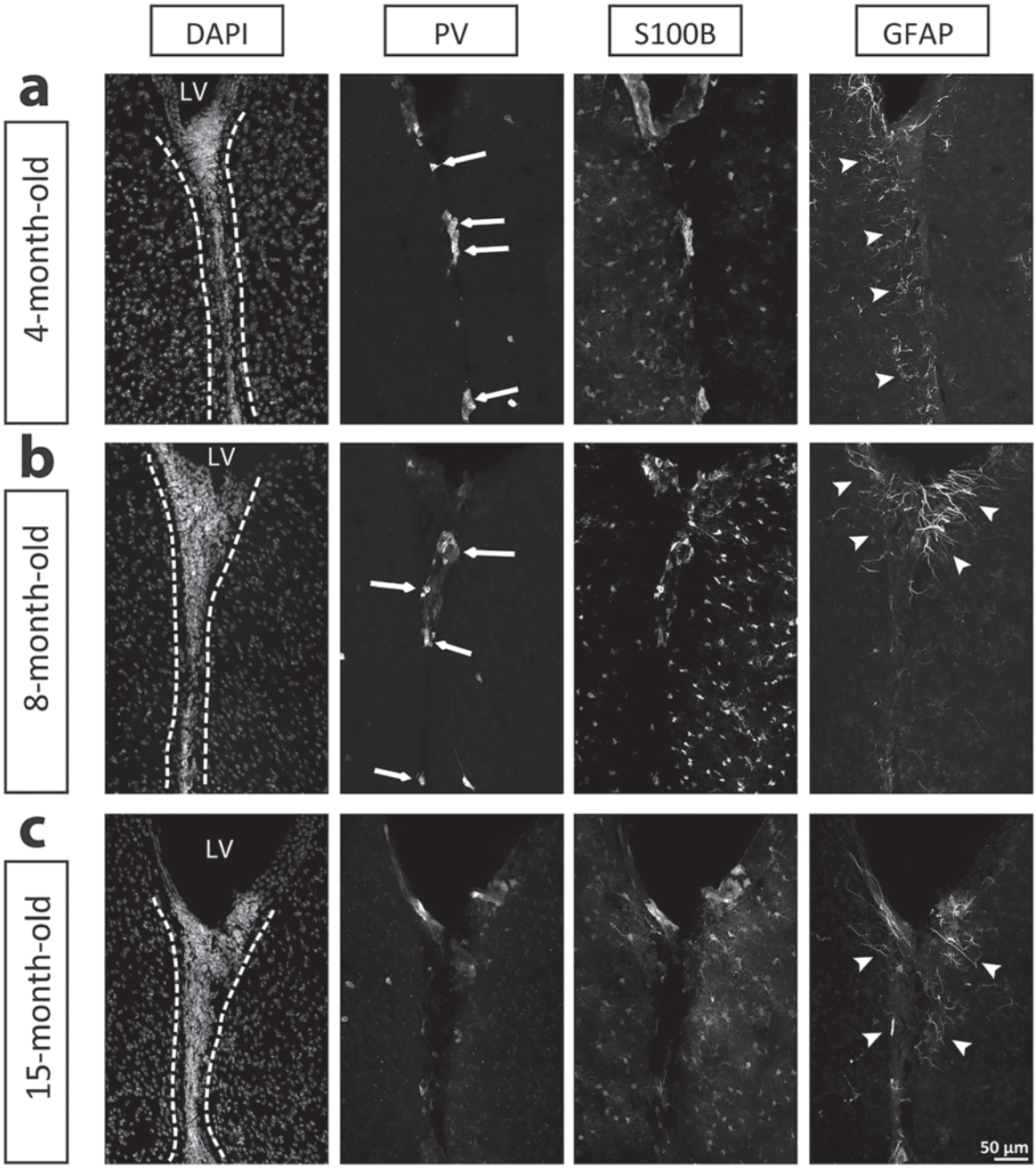

FIGURE 6 With aging, S100B+/PV+ ependymal cells decline in the LV-wall adhesions, whereas the distribution of ventricular gliosis undergoes spatial transposition. Confocal laser z-stack overprojection images of coronal sections from 4-month-old (a), 8-month-old (b), and 15-month-old (c) mice encompassing the regions of LV-wall adhesions (delineated by dashed lines) were immunostained for PV, S100B, and GFAP. Patches of S100B+/PV+ ependymal cells can be observed along the adhered ventricle walls in 4-month-old (a, arrows), respectively in 8-month-old mice (b, arrows). In 15-month-old mice, S100B+/PV+ cells are almost entirely lacking from the LV-wall adhesion zone (c). GFAP-immunostaining can be observed along the entire length of the adhering LV walls in 4-month-old mice (a, arrowheads). In 8-month-old mice, GFAP-stained processes are confined to the close vicinity of the LV (b, arrowheads), whereas it is largely lacking in the LV-wall adhesions. Similar is the situation in 15-month-old mice (c, arrowheads)

month-old (Figure 6b, arrows) mice, whereas such ependymal-cell populations were almost entirely lacking in 15-month-old mice (Figure 6c). This is in line with the observations that PV-staining intensity in the LV-wall adhesions correlates with adhesion volume—reflecting adhesion extent—in mice aged less than 10-month-old, but not in mice over 10 month of age, respectively with previous works that reported the disappearance of S100B+ ependymal cells from the LV-wall adhesions in 1-year-old mice (Shook et al., 2012).

GFAP-positive processes reflecting astrocytes could be found along the entire length of the LV-wall adhesions in 4-month-old mice (Figure 6a, arrowheads), whereas in 8- and 15-month-old mice GFAP+ astrocyte processes were found to be concentrated mostly

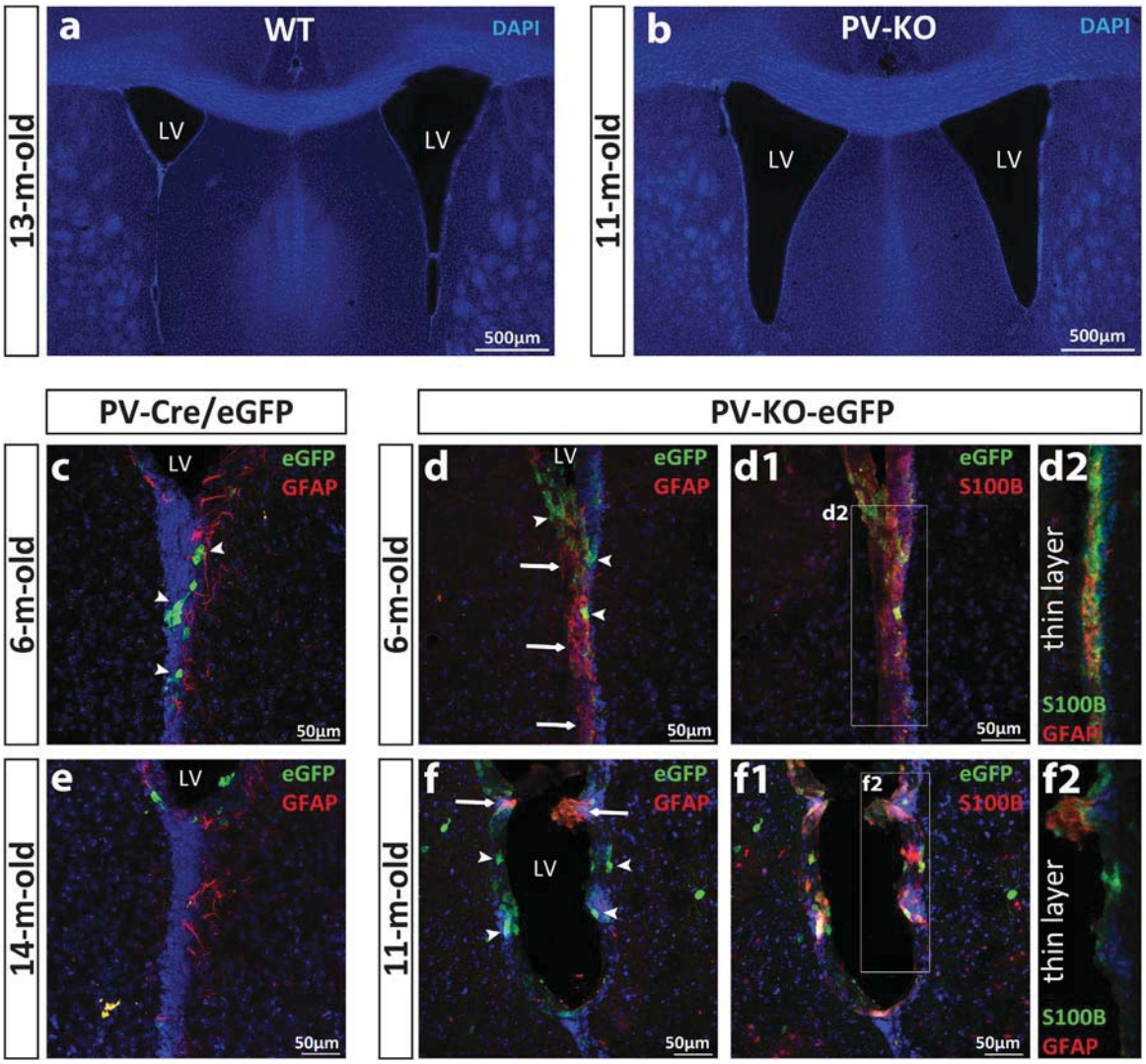

FIGURE 7 LV-wall adhesions of PV-KO-eGFP mice display crucial morphological alterations throughout aging. Low magnification image of a DAPI-counterstained coronal section at the level of the rostral portion of the LV reveals severe unilateral ventricle stenosis in a 13-month-old WT C57BL/6 mouse (a), whereas the LVs at approximately the same level display no adhesions in an 11-month-old PV-KO mouse (b). Confocal laser z-stack overprojection image of coronal sections encompassing the LV-wall adhesion region displays adhering LV walls with eGFP+ ependymal cells in the adhered ependymal layers in 6-month-old (c) and 14-month-old PV-Cre/eGFP (e) mice. Periventricular GFAP-immunopositive astrocyte processes can be found along the adhering ventricle walls (c, e), whereas eGFP+ cells are numerous in the LV-adhesion of 6-month-old (c, arrowheads) but virtually absent in the 14-month-old (e) PV-Cre/eGFP mouse. Confocal laser z-stack overprojection image in a 6-month-old PV-KO-eGFP mouse also demonstrates adhesions between the LV walls, with intensive GFAP (d, arrows) and S100B-immunostaining (d1) along the adhering ependymal layers. Several eGFP+ cells are present in the ependymal layers (d, arrowheads). Thin layer reconstruction of approx. 5 µm thickness depicts the S100B-positive ependymal layer to co-express GFAP (d2). Eleven-month-old PV-KO-eGFP mice display nonadhering LV walls with numerous eGFP+ cells in the ependymal layers (f, arrowheads). S100B-staining appears mostly intact in the 11-month-old PV-KO-eGFP mouse (f1), whereas some GFAP-stained patches can be found along the LV-wall thickenings (f, arrows). Thin layer z-reconstruction of S100B- and GFAP-immunostaining is shown in (f2)

around the ventricle-contacting areas of the LV-wall adhesions (Figure 6b,c, arrowheads). These findings suggest that LV-wall adhesions display some degree of gliosis along the adhering LV walls in early stages of ventricle stenosis, whereas later on periventricular gliosis is transposed to the surroundings of the ependymal layer that contacts the ventricle, and diminishes in the fused LV walls which lost ventricular contact.

3.6 | LV-wall adhesions of PV-KO-eGFP mice display crucial morphological alterations throughout aging

Next, we raised the question if PV-expressing ependymal cells in LV-wall adhesions contribute significantly to the progression of LV-wall fusions seen in aged mice. We found by visual observation that older PV-KO mice exhibited a reduced grade of ventricle stenosis than that of WT mice (Figure 7a,b). We also examined the LVs of PV-Cre/eGFP

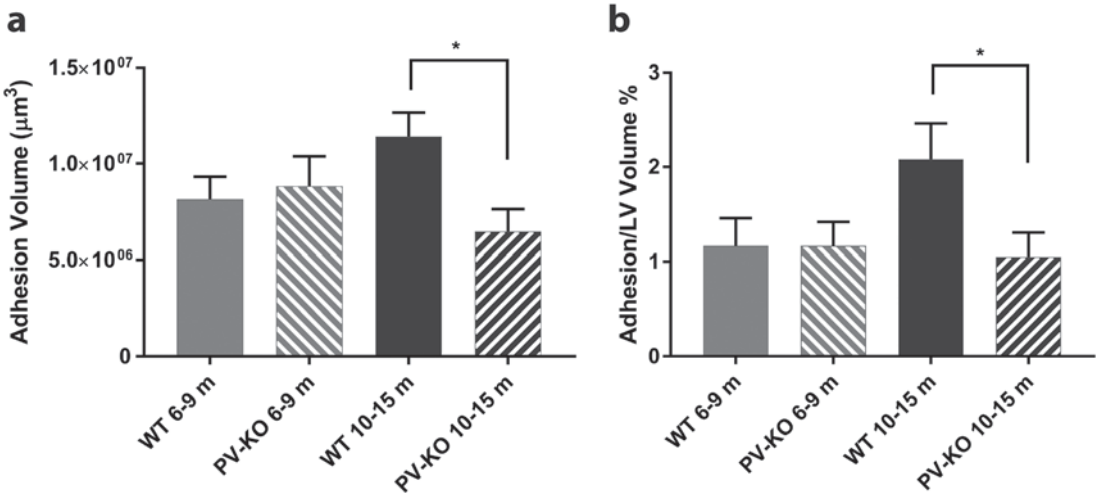

FIGURE 8 Mid-aged PV-KO mice exhibit lower grade of ventricle stenosis than their WT counterparts. The adhesion volume and rostral LV volume were measured by stereological volume estimation in PV-KO ($n = 18$) and WT ($n = 13$) mice and are represented as age-grouped mean values. We analyzed the region corresponding to the rostral part of the LV (approximately between Bregma levels +1.5 and 0 mm). No significant differences could be seen between younger (<10-month-old) PV-KO and WT mice (a, b); however, 10–15-month-old PV-KO mice displayed significantly lower adhesion volume (a), respectively adhesion volume/LV volume percentage (b) than did their WT counterparts. Statistical analyses were performed by one-way ANOVA and Kruskal-Wallis test. Error bars represent the SEM. $^*p < .05$

($n = 6$) and PV-KO-eGFP ($n = 5$) mice of different ages. When we compared nonaged (6-month-old) PV-KO-eGFP and PV-Cre/eGFP mice, we often found adhering medial and lateral LV walls in PV-KO-eGFP mice (Figure 7d); similarly to PV-Cre/eGFP ones of the same age (Figure 7c). In 6-month-old PV-KO-eGFP, numerous eGFP+ cells were present in the adhering ependymal layers (Figure 7d, arrowheads); moreover, the LV walls displayed extensive GFAP-immunostaining (Figure 7d, arrows). The LV walls also retained an intact S100B-staining, despite the presence of apparent adhesions (Figure 7d1). Thin z-plane reconstruction showed the S100B-positive ependymal layer to express GFAP (Figure 7d2). Six-month-old PV-Cre/eGFP mice formed LV-wall adhesions with evident ventricle stenosis, GFAP-stained periventricular astrocyte processes, and numerous eGFP+ cells in the LV-wall adhesions (Figure 7c, arrowheads). In aging (14-month-old) PV-Cre/eGFP mice, we found a severe grade of ventricle stenosis, GFAP-stained astrocytes around the LV walls, but virtually absent eGFP+ cells in the LV-wall adhesions (Figure 7e). These findings are in line with our observations described earlier (see Figure 6c). When we examined aging (11-month-old) PV-KO-eGFP mice, we found nonadhered LV walls with several "thickenings" in the ependymal layers (Figure 7f), which displayed patchy GFAP-immunostaining (Figure 7f, arrows, f2). Similarly to 6-month-old PV-KO-eGFP mice, numerous eGFP+ cells were found in the nonadhered LV walls (Figure 7f, arrowheads). Additionally, we found the LV walls to possess a virtually intact S100B-staining of the ependymal layers (Figure 7f1). These morphological differences between PV-Cre/eGFP and PV-KO-eGFP mice are quite striking: in PV-KO-eGFP, adhering LV walls displayed uniform GFAP-immunoreactivity, suggesting that the affected portions of the ependymal layer upregulated the astrocyte marker GFAP, unlike their WT counterparts. On the other hand, PV-KO-eGFP ependymal layers retained intact S100B-staining even in adhering LV walls, which could be explained if we assume that PV-KO adhesions less frequently formed persistent LV-wall fusions than those of WT mice. In line with this, PV-KO-eGFP ependymal layers displayed numerous eGFP+ cells even in older mice, suggesting that the *Pvalb* promoter remained active in these ependymal cells, but a permanent fusion of the LV walls did not yet occur. In other words, the progression of LV-wall adhesion into irreversible LV-wall fusions seems to be lacking or considerably delayed in PV-KO-eGFP mice, potentially due to the absence of a functional PV protein.

3.7 | Mid-aged PV-KO mice (10–15-month-old) has significantly reduced ventricle stenosis grade when compared to their WT counterparts

Next, we quantified and compared the adhesion volume and the LV volume in adult (6–15-month-old) WT C57BL/6 ($n = 13$) and PV-KO ($n = 18$) mice. We found that younger mice (6–9 month old) displayed no significant differences in adhesion volume [8,818,400 $\mu m^3 \pm 1{,}567{,}792$ SEM in PV-KO ($n = 10$) vs. 8,150,400 $\mu m^3 \pm 1{,}165{,}999$ SEM in WT ($n = 5$), see Figure 8a] or in adhesion volume/LV volume percentage ($1.164\% \pm 0.2546$ SEM in PV-KO vs. $1.163\% \pm 0.2963$ SEM in WT, see Figure 8b). However, we found a 43.3% reduction in adhesion volume [6,471,000 $\mu m^3 \pm 1{,}169{,}527$ SEM in PV-KO ($n = 8$) vs. $11{,}406{,}000 \pm 1{,}264{,}634$ SEM in WT, ($n = 8$), $p = .0282$, see Figure 8a]; and a 49.6% reduction in adhesion volume/LV volume percentage ($1.048\% \pm 0.2583$ SEM in PV-KO vs. $2.079\% \pm 0.3809$ in WT, $p = .0221$, see Figure 8b) in older (10–15-month old) PV-KO mice when compared to their WT counterparts. When we compared the age-grouped values in the same genotype, we found no significant differences between younger and mid-aged WT mice, or between younger and mid-aged PV-KO mice. A tendency of increase in adhesion volume and adhesion volume/LV volume percentage in mid-

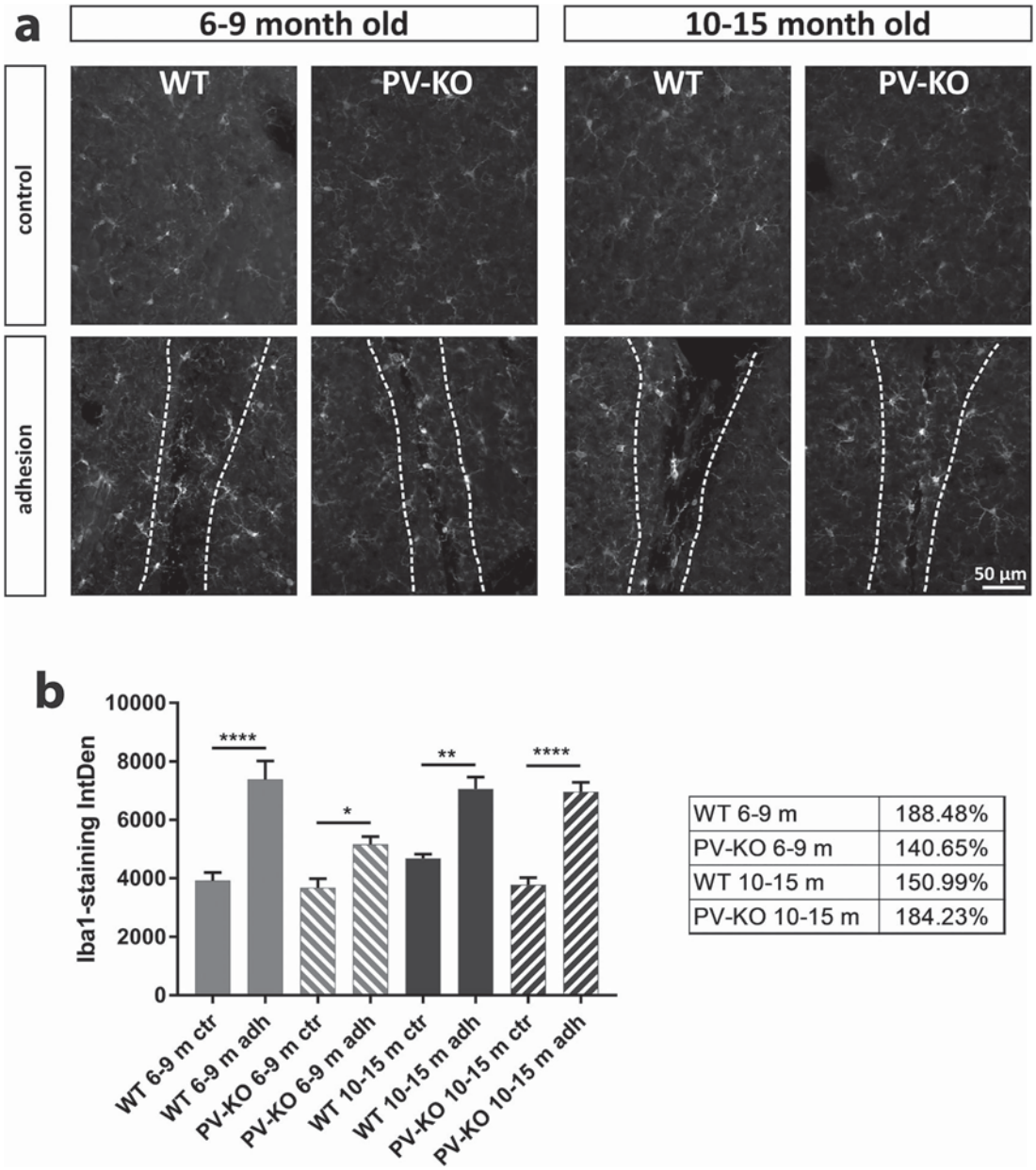

WT 6-9 m	188.48%
PV-KO 6-9 m	140.65%
WT 10-15 m	150.99%
PV-KO 10-15 m	184.23%

FIGURE 9 Microglia is activated in the LV-wall adhesion in both WT and PV-KO mice, however, at different extent between age groups. Fluorescent micrographs displaying Iba1-immunostaining on coronal sections—at the level of LV-wall adhesions—of age-grouped PV-KO and WT C57BL/6 mice show visibly more enhanced Iba1-immunofluorescence in the adhesion zone (marked by dashed lines) than in the control region of the striatum in each of the presented age groups and genotypes (a). Iba1-immunofluorescence intensity (integrated density—IntDen) was quantified on a series of ROIs in the control, respectively adhesion regions following threshold adjustment and particle analysis by ImageJ. In the graph, IntDen is displayed as mean IntDen values following averaging (b). Significant increase of Iba1-immunofluorescence is seen in the LV-adhesions of each group when compared to the control region (b). The table shows the IntDen adh/ctr percentage values in the different age groups. Statistical analysis was performed by Kruskal-Wallis test. Error bars show SEM. adh = adhesion; ctr = control. $^{*}p < .05$, $^{**}p < .005$, $^{****}p < .0001$

aged WT, respectively a tendency of decrease in mid-aged PV-KO could be observed, however, the differences were not significant. The finding that mid-aged PV-KO exhibit reduced grade of ventricle stenosis when compared to WT is in line with our other observations in this study, and suggests an involvement of PV-expressing ependymal cells in the formation of permanent fusions between the medial and lateral LV walls, thereby, in the progression of aging-associated ventricle stenosis.

3.8 | Microglial activation was observed in both PV-KO and WT LV-wall adhesions, with a delay in PV-KO mice

We postulated that at some point during the progression of fusion between medial and lateral LV walls microglial activation was implicated, since microglial cells were previously shown to exhibit robust activation, phagocytosis of ependymal debris and migration upon

periventricular damage (Carbonell, Murase, Horwitz, & Mandell, 2005). The increased expression level of the microglia marker Iba1 was shown to be associated with microglial activation (Ito, Tanaka, Suzuki, Dembo, & Fukuuchi, 2001), therefore, we quantified Iba1-immunoreactivity in adult PV-KO and WT mice in the LV-wall adhesions and in the striatum as control in the different age groups (Figure 9a). Iba1-immunofluorescence—measured as integrated density (IntDen) by ImageJ upon threshold adjustment in defined ROIs (268.57 μm × 307.62 μm)—of the LV-wall adhesions was compared to the control Iba1-staining in the striatum on the same sections. We found a significant increase of Iba1-immunoreactivity in the LV-adhesions in both younger (6–9 month-old) and older (10–15 month-old) WT and PV-KO mice (Figure 9b). The degree of increase was however somewhat different between the age groups: 6–9 month-old WT mice displayed a 188.48% increase ($p < .0001$) in IntDen in the LV-wall adhesion when compared to the Iba1-immunofluorescence of the striatum, whereas 10–15 month-old WT displayed a 150.99% increase ($p = .0033$). In PV-KO mice, younger animals (6–9 month-old) exhibited a 140.65% increase ($p = .0426$), and mid-aged mice (10–15 month-old) a 184.23% increase ($p < .0001$) (Figure 9b). These findings reflect a slight, ca. 20% decrease in microglial activity in LV-wall adhesions of mid-aged mice compared to younger ones in WT, whereas a ca. 130% increase in mid-aged PV-KO mice compared to younger PV-KO mice, suggesting a time-shift in microglial activity in the region of LV-wall adhesions when PV is lacking from ependymal cells. This could be explained by a delay in the formation of LV-wall fusions in PV-KO, resulting in a later on-set of microglial recruitment in the affected areas.

4 | DISCUSSION

We found PV-immunopositive ependymal cells in the adhered layers of the rostral LV walls of nonaged WT mice, which co-expressed the ependymal cell marker S100B and displayed a reactive phenotype similar to injury-reactive ependymal cells described in our previous study (Szabolcsi & Celio, 2015). The aim of our study was to investigate the relevance of PV-positive ependymal cells in LV-wall adhesions. We found that periventricular PV-immunoreactivity correlated to the grade of LV stenosis in mice younger than 10 month of age. In line with this observation, we found significantly lower grade of ventricle stenosis in older PV-KO mice, suggesting that PV-expressing ependymal cells contribute to the early stages of the formation of LV-wall fusions, and consequently to the progression of LV stenosis. We observed that throughout aging, as adhesion/fusion of the LV walls progresses, PV-expressing ependymal cells diminished from the LV-wall fusions. We quantified the grade of ventricle stenosis of PV-KO and C57BL/6 WT mice, and found significantly lower adhesion extent and stenosis grade in mid-aged (>10-month-old) PV-KO mice when compared to their WT counterparts, whereas no difference was found between younger (<10-month-old) PV-KO and WT mice. Thus, our findings highlight an important involvement of PV-expressing ependymal cells found in adhering LV walls in the aging-associated progression of ventricle stenosis.

During the course of ventricle stenosis, mice develop fusions of the medial and lateral LV walls with a resulting deterioration of the initially intact ependymal layer and most importantly, a decline of the functional proliferative zone in the affected SVZ in the regions of the LV-wall fusions (Luo et al., 2006; Shook et al., 2012). Ependymal cells lining brain ventricles display only limited regenerative capacities since they are fully differentiated (Spassky et al., 2005), and they have been shown to irreversibly disappear from the ventricle wall adhesions throughout aging (Shook et al., 2012). Considering this together with the loss of neurogenic SVZ in the adhesions, LV-wall adhesions significantly contribute to the pathophysiology of aging. The mechanisms and precise cellular interplay which ultimately lead to the adhesion of the LV walls remain unknown, but we demonstrate here that adhering, PV-expressing ependymal cells are implicated in this process, whereas periventricular gliosis does not seem to play a crucial role.

Several factors could be involved in the progression of LV-wall fusions. Some ependymal-cell responses to deleterious effects have been investigated and stressed the importance of the maintenance of an intact ependymal lining. In the aging SVZ, dying ependymal cells are replaced by dividing astrocytes, probably to maintain an intact CSF-SVZ barrier (Luo et al., 2008). On the other hand, excessive loss of ependymal cells results in extensive gliosis at the ventricle surface with following ventriculomegaly (Shook et al., 2013). Ventricle enlargement in the human brain has been attributed to neurological/psychiatric illnesses (Palha et al., 2012); however, Shook et al. showed that ependymal loss and consequent periventricular gliosis alone could lead to ventriculomegaly, independent of neurodegeneration. Thus, the integrity of the ventricle barrier formed by the ependymal monolayer is crucial to maintain the normal volume of the brain ventricles. Nevertheless, the rate of production and absorption of CSF might also alter the brain ventricle volume, potentially leading to ventriculomegaly or ventricle stenosis. Alterations in the microarchitecture of the SVZ might also contribute to events that compromise the barrier integrity. Ependymal-cell responses to these factors might be very variable.

Mature ependymal cells in the brain do not reenter the cell cycle under normal conditions; however, they have been shown to generate new neurons and glial cells upon disruption of Notch signaling (Carlen et al., 2009). Nevertheless, they fail the "stemness" criteria due to their incapability of self-renewal. Thus, their primary role in the brain seems to lay in providing an important barrier between CSF and brain parenchyma. We have recently described the injury-induced PV-upregulation in ependymal cells, which displayed reactive phenotype, enhanced cell motility and wound-closure capacity upon PV-expression (Szabolcsi & Celio, 2015). We showed that such PV-expression in ependymal cells was NF-κB signaling dependent and could be modulated by altering the level of oxidative stress, thus implicating injury-induced inflammation in this process. We also found previously that injury-reactive ependymal cells acquired a reactive phenotype, which resembles that of ependymal cells in the LV-wall adhesions described in our present study. This suggests that ependymal cells that undergo disintegration due to either mechanical lesion or adhesions of the LV walls react in similar ways: with PV-upregulation

and phenotype shift from cuboidal, epithelial-like cells to bipolar cell morphology with elongated processes.

This type of reaction of challenged ependymal cells might be caused by an altered extracellular milieu and cellular interplay that accompanies tissue remodeling, such as cytokines released by activated microglial cells. In our present study, we indeed found activated microglial cells in the zone of LV-wall adhesions and fusions, supporting a possible role for microglia-mediated factors in the observed alteration of ependymal cells. However, microglial activation could also be a consequence rather than a cause of reactive ependymal phenotype. Reactive ependymal cells might also exert antigen-presenting functions and thereby facilitate microglial recruitment.

Nevertheless, the molecular triggers underlying ventricle stenosis, respectively those inducing a reactive phenotype in ependymal cells are as yet unknown. The disruption of the liquor-brain barrier upon disintegration of the ependymal monolayer by mechanical lesion or fusion of the opposite LV walls might generate increased cellular stress that switch on defensive cell mechanisms in this cell type. Additionally, losing contact to neighboring ependymal cells might lead to a loss of apical-basal polarity and changes in cell shape, that is, to a loss of epithelial-like phenotype. Given that the ependymal layer, unlike other epithelial linings, is nonregenerative; the capacity of ependymal cells for local remodeling is very limited. Stretching of ependymal cells in enlarged ventricles has been observed (Shook et al., 2013), but the responses of ependymal cells to the disruption of the ependymal monolayer remain largely unknown. In response to lesion or disruption of Notch-signaling, ependymal cells in the region of the neurogenic LV walls can convert into astrocytes and vice versa, confirming that ependymal-cell characteristics are actively maintained by constitutive Notch-signaling (Carlen et al., 2009; Nomura et al., 2010). However, the ependymal-to-astrocyte transition implicated novel GFAP-expression in the cellular processes (Nomura et al., 2010), which was not the case in LV-wall adhesion ependymal cells: we did not find co-existence of GFAP-staining in the cellular processes of PV+ reactive ependymal cells. However, PV-KO-eGFP ependymal cells in the LV-wall adhesion did express GFAP (Figure 7d,d2), which might hint at an alternative mechanism of "activation" when PV is absent from ependymal cells. One explanation for the lower grade of ventricle stenosis observed in mid-aged PV-KO mice could be a slower progression of ventricle stenosis caused by insufficient activation or a delay in acquiring the reactive phenotype seen in PV-expressing WT ependymal cells.

Why do ependymal cells upregulate PV? PV is an EF-hand calcium-binding protein known as a slow-onset calcium buffer with high calcium-binding affinity. PV is abundantly expressed in the brain, mostly in fast-spiking GABAergic interneurons (Celio, 1986) but also in long projection neurons (Bilella, Alvarez-Bolado, & Celio, 2016), where its role is extensively studied, however, very little is known about PV in other elements of the nervous system. Calcium buffers such as PV are believed to alter the spatiotemporal aspects of calcium transients (Schwaller, Meyer, & Schiffmann, 2002). Some calcium-signaling related mechanisms could also be involved in the case of reactive phenotype shift seen in ependymal cells, however, the spectrum of biological processes that are dependent on calcium-signaling are endless. The cell shape alterations seen in LV-wall adhesion ependymal cells are similar to those seen in injury-reactive ependymal cells (Szabolcsi & Celio, 2015), therefore, we could assume that PV-upregulation implies similar processes in the case of LV-wall adhesion ependymal cells as well, such as cytoskeletal remodeling and cell motility. However, the precise molecular pathways where PV could interact are yet to be discovered.

In our present study, we demonstrate for the first time an ependymal-cell response triggered by the fusion of the opposite LV walls that involves PV-upregulation and reactive phenotype shift in ependymal cells in the affected regions. PV-positive ependymal cells seem to contribute to the propagation of adhesion- and fusion-formation observed throughout aging, based on our observation of lower ventricle stenosis grade in aging PV-KO mice. The development of ventricle stenosis associated to severe decline in adult neurogenesis throughout aging is poorly understood, our study therefore sheds light on a novel aspect of this biological feature of aging.

ACKNOWLEDGMENTS

The authors would like to thank Felix Meyenhofer for IT and data management support, Christiane Marti, Laurence Clement, Marlène Sanchez, and Martine Steinauer for the laboratory assistance and Simone Eichenberger for the animal care. This work was supported by the Swiss Multiple Sclerosis Society (grant no. 2016–28) and the Forschungsfonds of the University of Fribourg (grant no. 582).

CONFLICT OF INTEREST

The authors declare that there is no conflict of interest regarding the publication of this article.

AUTHOR CONTRIBUTION

All authors had full access to all the data in the study and take responsibility for the integrity of the data and the accuracy of the data analysis. Study concept and design: VS. Acquisition of data: VS, FF and AB. Analysis and interpretation of data: VS, FF, MRC and WB. Drafting of the manuscript: VS, FF, and MRC. Critical revision of the manuscript for important intellectual content: VS, WB, MRC, and FF. Statistical analysis: VS. Obtained funding: VS. Administrative, technical, and material support: VS and MRC. Study supervision: VS.

REFERENCES

Alvarez, J. I., & Teale, J. M. (2007). Differential changes in junctional complex proteins suggest the ependymal lining as the main source of leukocyte infiltration into ventricles in murine neurocysticercosis. *Journal of Neuroimmunology*, *187*(1–2), 102–113. doi:10.1016/j.jneuroim.2007.05.005

Bilella, A., Alvarez-Bolado, G., & Celio, M. R. (2016). The Foxb1-expressing neurons of the ventrolateral hypothalamic parvafox nucleus project to defensive circuits. *Journal of Comparative Neurology*, *524*(15), 2955–2981. doi:10.1002/cne.24057

Bosco, A., Steele, M. R., & Vetter, M. L. (2011). Early microglia activation in a mouse model of chronic glaucoma. *Journal of Comparative Neurology*, *519*(4), 599–620. doi:10.1002/cne.22516

Brai, E., Marathe, S., Zentilin, L., Giacca, M., Nimpf, J., Kretz, R., ... Alberi, L. (2014). Notch1 activity in the olfactory bulb is odour-dependent and contributes to olfactory behaviour. *European Journal of Neuroscience*, *40*(10), 3436–3449. doi:10.1111/ejn.12719

Carbonell, W. S., Murase, S. I., Horwitz, A. F., & Mandell, J. W. (2005). Infiltrative microgliosis: Activation and long-distance migration of subependymal microglia following periventricular insults. *Journal of Neuroinflammation*, *2*(1), 5. doi:10.1186/1742-2094-2-5

Carlen, M., Meletis, K., Goritz, C., Darsalia, V., Evergren, E., Tanigaki, K., ... Frisen, J. (2009). Forebrain ependymal cells are Notch-dependent and generate neuroblasts and astrocytes after stroke. *Nature Neuroscience*, *12*(3), 259–267.

Celio, M. R. (1986). Parvalbumin in most gamma-aminobutyric acid-containing neurons of the rat cerebral cortex. *Science*, *231*(4741), 995–997.

Cocchia, D. (1981). Immunocytochemical localization of S-100 protein in the brain of adult rat. An ultrastructural study. *Cell and Tissue Research*, *214*(3), 529–540.

Conover, J. C., & Shook, B. A. (2011). Aging of the subventricular zone neural stem cell niche. *Aging and Disease*, *2*(1), 49–63.

Del Bigio, M. R. (2010). Ependymal cells: Biology and pathology. *Acta Neuropathologica*, *119*(1), 55–73.

Doetsch, F., & Alvarez-Buylla, A. (1996). Network of tangential pathways for neuronal migration in adult mammalian brain. *Proceedings of the National Academy of Sciences of the United States of America*, *93*(25), 14895–14900.

Enwere, E., Shingo, T., Gregg, C., Fujikawa, H., Ohta, S., & Weiss, S. (2004). Aging results in reduced epidermal growth factor receptor signaling, diminished olfactory neurogenesis, and deficits in fine olfactory discrimination. *Journal of Neuroscience*, *24*(38), 8354–8365. doi:10.1523/JNEUROSCI.2751-04.2004

Filice, F., Vorckel, K. J., Sungur, A. O., Wohr, M., & Schwaller, B. (2016). Reduction in parvalbumin expression not loss of the parvalbumin-expressing GABA interneuron subpopulation in genetic parvalbumin and shank mouse models of autism. *Molecular Brain*, *9*, 10. doi: 10.1186/s13041-016-0192-8

Ford, M. C., Grothe, B., & Klug, A. (2009). Fenestration of the calyx of held occurs sequentially along the tonotopic axis, is influenced by afferent activity, and facilitates glutamate clearance. *Journal of Comparative Neurology*, *514*(1), 92–106. doi:10.1002/cne.21998

Gundersen, H. J., & Jensen, E. B. (1987). The efficiency of systematic sampling in stereology and its prediction. *Journal of Microscopy*, *147* (Pt 3), 229–263.

Hiroyasu, S., Ozawa, T., Kobayashi, H., Ishii, M., Aoyama, Y., Kitajima, Y., ... Tsuruta, D. (2013). Bullous pemphigoid IgG induces BP180 internalization via a macropinocytic pathway. *The American Journal of Pathology*, *182*(3), 828–840. doi:10.1016/j.ajpath.2012.11.029

Ito, D., Imai, Y., Ohsawa, K., Nakajima, K., Fukuuchi, Y., & Kohsaka, S. (1998). Microglia-specific localisation of a novel calcium binding protein, Iba1. *Brain Research. Molecular Brain Research*, *57*(1), 1–9.

Ito, D., Tanaka, K., Suzuki, S., Dembo, T., & Fukuuchi, Y. (2001). Enhanced expression of Iba1, ionized calcium-binding adapter molecule 1, after transient focal cerebral ischemia in rat brain. *Stroke*, *32* (5), 1208–1215.

Jacquet, B. V., Salinas-Mondragon, R., Liang, H., Therit, B., Buie, J. D., Dykstra, M., ... Ghashghaei, H. T. (2009). FoxJ1-dependent gene expression is required for differentiation of radial glia into ependymal cells and a subset of astrocytes in the postnatal brain. *Development*, *136*(23), 4021–4031.

Kaplan, M. S., & Hinds, J. W. (1977). Neurogenesis in the adult rat: Electron microscopic analysis of light radioautographs. *Science*, *197* (4308), 1092–1094.

Lois, C., & Alvarez-Buylla, A. (1994). Long-distance neuronal migration in the adult mammalian brain. *Science*, *264*(5162), 1145–1148.

Luo, J., Daniels, S. B., Lennington, J. B., Notti, R. Q., & Conover, J. C. (2006). The aging neurogenic subventricular zone. *Aging Cell*, *5*(2), 139–152. doi:10.1111/j.1474-9726.2006.00197.x

Luo, J., Shook, B. A., Daniels, S. B., & Conover, J. C. (2008). Subventricular zone-mediated ependyma repair in the adult mammalian brain. *Journal of Neuroscience*, *28*(14), 3804–3813.

Mirzadeh, Z., Han, Y. G., Soriano-Navarro, M., Garcia-Verdugo, J. M., & Alvarez-Buylla, A. (2010). Cilia organize ependymal planar polarity. *Journal of Neuroscience*, *30*(7), 2600–2610.

Mirzadeh, Z., Merkle, F. T., Soriano-Navarro, M., Garcia-Verdugo, J. M., & Alvarez-Buylla, A. (2008). Neural stem cells confer unique pinwheel architecture to the ventricular surface in neurogenic regions of the adult brain. *Cell Stem Cell*, *3*(3), 265–278.

Nomura, T., Goritz, C., Catchpole, T., Henkemeyer, M., & Frisen, J. (2010). EphB signaling controls lineage plasticity of adult neural stem cell niche cells. *Cell Stem Cell*, *7*(6), 730–743.

Ostrowski, L. E., Hutchins, J. R., Zakel, K., & O'Neal, W. K. (2003). Targeting expression of a transgene to the airway surface epithelium using a ciliated cell-specific promoter. *Molecular Therapy*, *8*(4), 637–645.

Paez-Gonzalez, P., Abdi, K., Luciano, D., Liu, Y., Soriano-Navarro, M., Rawlins, E., ... Kuo, C. T. (2011). Ank3-dependent SVZ niche assembly is required for the continued production of new neurons. *Neuron*, *71*(1), 61–75.

Palha, J. A., Santos, N. C., Marques, F., Sousa, J., Bessa, J., Miguelote, R., ... Belmonte-de-Abreu, P. (2012). Do genes and environment meet to regulate cerebrospinal fluid dynamics? Relevance for schizophrenia. *Frontiers in Cellular Neuroscience*, *6*, 31. doi:10.3389/fncel.2012.00031

Petkau, T. L., Neal, S. J., Orban, P. C., MacDonald, J. L., Hill, A. M., Lu, G., ... Leavitt, B. R. (2010). Progranulin expression in the developing and adult murine brain. *Journal of Comparative Neurology*, *518*(19), 3931–3947. doi:10.1002/cne.22430

Raponi, E., Agenes, F., Delphin, C., Assard, N., Baudier, J., Legraverend, C., & Deloulme, J. C. (2007). S100B expression defines a state in which GFAP-expressing cells lose their neural stem cell potential and acquire a more mature developmental stage. *Glia*, *55*(2), 165–177. doi:10.1002/glia.20445

Sawamoto, K., Wichterle, H., Gonzalez-Perez, O., Cholfin, J. A., Yamada, M., Spassky, N., ... Alvarez-Buylla, A. (2006). New neurons follow the flow of cerebrospinal fluid in the adult brain. *Science*, *311*(5761), 629–632.

Schwaller, B., Dick, J., Dhoot, G., Carroll, S., Vrbova, G., Nicotera, P., ... Celio, M. R. (1999). Prolonged contraction-relaxation cycle of fast-twitch muscles in parvalbumin knockout mice. *American Journal of Physiology*, *276*(2 Pt 1), C395–C403.

Schwaller, B., Meyer, M., & Schiffmann, S. (2002). 'New' functions for 'old' proteins: The role of the calcium-binding proteins calbindin D-28k, calretinin and parvalbumin, in cerebellar physiology. Studies with knockout mice. *Cerebellum*, *1*(4), 241–258.

Shook, B. A., Lennington, J. B., Acabchuk, R. L., Halling, M., Sun, Y., Peters, J., ... Conover, J. C. (2013). Ventriculomegaly associated with ependymal gliosis and declines in barrier integrity in the aging human and mouse brain. *Aging Cell*, *13*(2), 340–350.

Shook, B. A., Manz, D. H., Peters, J. J., Kang, S., & Conover, J. C. (2012). Spatiotemporal changes to the subventricular zone stem cell pool through aging. *Journal of Neuroscience*, *32*(20), 6947–6956. doi: 10.1523/JNEUROSCI.5987-11.2012

Sofroniew, M. V., & Vinters, H. V. (2010). Astrocytes: Biology and pathology. *Acta Neuropathologica*, *119*(1), 7–35. doi:10.1007/s00401-009-0619-8

Spassky, N., Merkle, F. T., Flames, N., Tramontin, A. D., Garcia-Verdugo, J. M., & Alvarez-Buylla, A. (2005). Adult ependymal cells are postmitotic and are derived from radial glial cells during embryogenesis. *Journal of Neuroscience*, *25*(1), 10–18.

Szabolcsi, V., Albisetti, G. W., & Celio, M. R. (2017). Parvalbumin-neurons of the ventrolateral hypothalamic parvafox nucleus receive a glycinergic input: A gene-microarray study. *Frontiers in Molecular Neuroscience*, *10*, 8. doi:10.3389/fnmol.2017.00008

Szabolcsi, V., & Celio, M. R. (2015). De novo expression of parvalbumin in ependymal cells in response to brain injury promotes ependymal remodeling and wound repair. *Glia*, *63*(4), 567–594. doi:10.1002/glia.22768

Tropepe, V., Craig, C. G., Morshead, C. M., & van der Kooy, D. (1997). Transforming growth factor-alpha null and senescent mice show decreased neural progenitor cell proliferation in the forebrain subependyma. *Journal of Neuroscience*, *17*(20), 7850–7859.

Waters, J. C. (2009). Accuracy and precision in quantitative fluorescence microscopy. *The Journal of Cell Biology*, *185*(7), 1135–1148. doi:10.1083/jcb.200903097

Xu, X., Roby, K. D., & Callaway, E. M. (2010). Immunochemical characterization of inhibitory mouse cortical neurons: Three chemically distinct classes of inhibitory cells. *Journal of Comparative Neurology*, *518*(3), 389–404. doi:10.1002/cne.22229

Young, C. C., van der Harg, J. M., Lewis, N. J., Brooks, K. J., Buchan, A. M., & Szele, F. G. (2013). Ependymal ciliary dysfunction and reactive astrocytosis in a reorganized subventricular zone after stroke. *Cereb Cortex*, *23*(3), 647–659.

How to cite this article: Filice F, Celio MR, Babalian A, Blum W, Szabolcsi V. Parvalbumin-expressing ependymal cells in rostral lateral ventricle wall adhesions contribute to aging-related ventricle stenosis in mice. *J Comp Neurol*. 2017;525:3266–3285. https://doi.org/10.1002/cne.24276